Universität Bremen

Bachelor Thesis

Department of Geosciences

University of Bremen

Tracing permafrost input into the Laptev Sea by compound specific analyses of *n*-alkanoic acids

Author: Laura Kattein

1st Supervisor: Prof. Dr. Gesine Mollenhauer
2nd Supervisor: Dr. Enno Schefuß
Date of Submission: 22.05.2018

Erklärung gem. § 8 Abs. 9 AT der Bachelor-PO der Universität Bremen

Ich versichere hiermit, dass ich meine Bachelorarbeit selbständig verfasst und keine anderen als die angegebenen Quellen und Hilfsmittel benutzt habe. Wörtliche oder dem Sinn nach aus anderen Werken entnommene Stellen habe ich unter Angabe der Quellen kenntlich gemacht. Dies gilt auch für Internetquellen.

Weiterhin erkläre ich, dass die Bachelorarbeit in unveränderter Fassung der Öffentlichkeit zur Verfügung gestellt werden kann.

Ort/Datum: _____

Unterschrift: _____

Table of Content

Abstract

To investigate effects of permafrost thaw on the sedimentary inventory of the Arctic Ocean, two cores recovered off the coast of the Lena delta were studied. Compound specific analyses of *n*-alkanoic acids were conducted to obtain information about the different sources contributing to the sediment. Stable carbon and hydrogen isotope ratios were measured using ion ratio mass spectrometry, while the radiocarbon content was determined using compound specific radiocarbon analysis. A blank and methyl correction was performed to determine the radiocarbon content at the time of deposition.

Radiocarbon analyses yield generally higher ages for long-chain *n*-alkanoic acids, compared to short-chain ones. Two alkanoic acids ($C_{16:0}$ and $C_{28:0}$) used as biomarkers for marine and terrestrial input were chosen to investigate differences in the sources contributing to each core site. Hydrogen isotope ratios and radiocarbon measurements of the terrestrial biomarker suggest a topsoil permafrost dominated input of organic matter. Two binary mixing models yield similar results for the proportions of contributing sources. There was no evidence for a change of these ratios over the course of the last century.

Differences in the concentration profiles of $C_{16:0}$ in the two cores suggest different degradation rates in the two cores, which is supported by previously published data.

Based on the stable hydrogen isotope ratios of the terrestrial biomarker, there is indication for an increased contribution of topsoil-permafrost derived organic matter from a more southern location in the catchment. A distinct influence of excess ^{14}C produced during nuclear weapon tests is reflected in the radiocarbon content of the $C_{16:0}$ samples of one core.

List of Figures

List of Tables

List of Abbreviations

AMS	Accelerated Mass Spectrometry
BWOC	Bottom Water Oxygen Concentration
CRS	Constant Rate of Supply
CSRA	Compound Specific Radiocarbon Analysis
DCM	Dichloromethane
GC	Gas Chromatography
GC-FID	Gas Chromatography Flame Ionization Detector
GC-IRMS	Gas Chromatography Isotope Ratio Mass Spectrometry
GC-MS	Gas Chromatography Mass Spectrometry
EA	Element Analyzer
HEX	Hexane
HMW	High Molecular Weight
ICD-PF	Ice Complex Deposit Permafrost
MeOH	Methanol
MICADAS	MIni CArbon DAting System
OM	Organic Matter
Prep-GC	Preparative Gas Chromatography
SIM	Single Ion Mode
TC	Total Carbon
TLE	Total Lipid Extract
TN	Total Nitrogen
TOC	Total Organic Carbon
TS-PF	Topsoil Permafrost

1 Introduction

1.1 Impact of climate change on arctic permafrost

Arctic regions and the northern high latitudes are of outstanding importance to the global atmospheric and marine carbon cycle. As shown in Figure 1 an estimated quarter of the Northern Hemisphere's land mass is underlain by permafrost (Zhang et al., 2003), which is defined as soil, rock or sediment that remains frozen for at least two consecutive years. Depending on the area coverage, permafrost is classified as continuous (> 90%), discontinuous (50-90%), sporadic (10-50%) or isolated (<10%).

The surficial soil layer of permafrost is subject to annual thaw-freeze cycles and therefore referred to as the active layer (Burn, 1998). Permafrost stores an estimated 50% of the global subterranean organic carbon (Hugelius et al., 2014; Tarnocai et al., 2009).

The perennially frozen carbon pool is excluded from carbon cycling, but most likely has the capability to persistently influence both arctic and global carbon cycles if it is released. Climatic response to the release of carbon largely depends on the proportion of carbon that is transferred into other carbon sequestering pools (i.e. marine sediments) in contrast to carbon that is subject to soil respiration. Organic carbon that is available for soil respiration is converted into CO_2 and CH_4, which, upon release into the atmosphere, results in positive climate feedback (Schuur et al., 2008; Walter et al., 2006). It is therefore crucial to understand the fate of permafrost derived organic carbon, in order to estimate its impact on the carbon cycles.

The arctic is especially vulnerable to global climate change (McGuire et al., 2009) and numerous large-scale effects such as active layer deepening (Yi et al., 2018), increased arctic river runoff (Tananaev et al., 2016) and decreased permafrost extent (Jorgenson et al., 2001) have been perceptible.
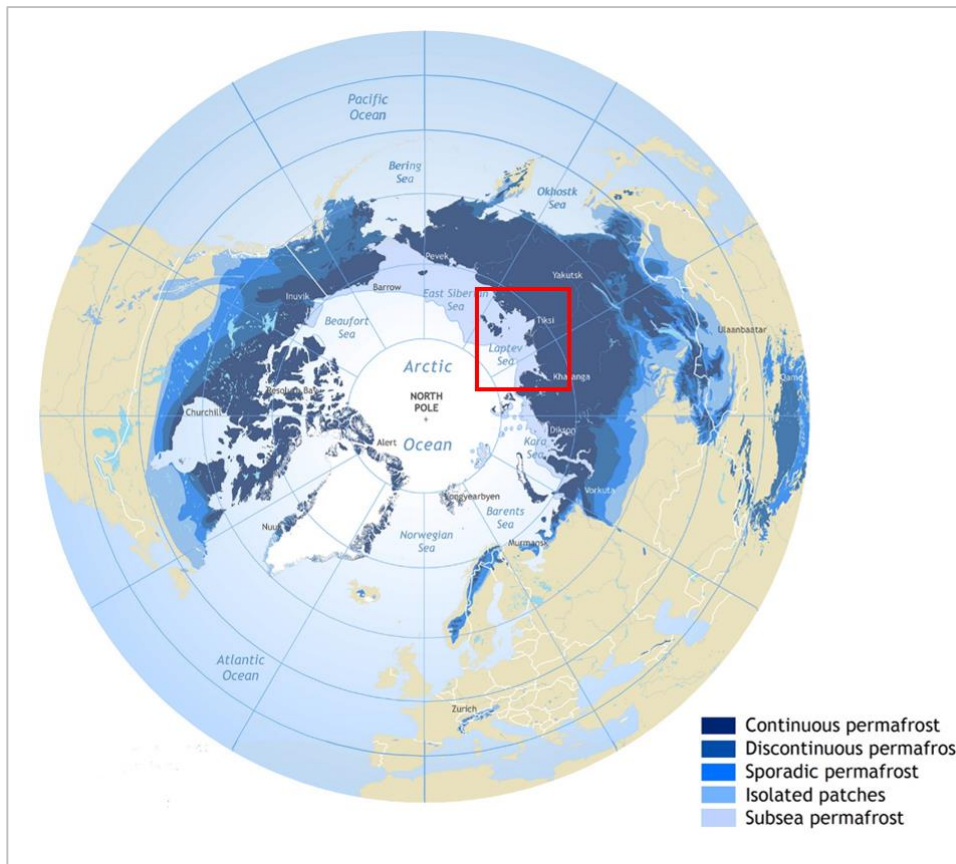
Figure 1: Distribution of different types of permafrost across the northern hemisphere (Brown et al., 1997). The red square shows the study area.

1.2 Study area

The river Lena is one of the largest Russian Arctic Rivers, draining a watershed of 2,430,000 km^2 into the Laptev Sea, a marginal sea of the Arctic Ocean. Upon flowing into the Laptev Sea, the river branches in more than 150 channels, forming the largest delta (30,000km^2) in the Arctic (Costard & Gautier, 2007). The river discharges 585 km^3 of water (mean over the years 2000-2012) (ArcticGRO Discharge Dataset, www.arcticgreatrivers. org, retrieved 10 April 2018) and 24 Mt of sediment (Alabyan et al., 1995) per year, mostly through the three main channels Olenekskaya, Bykovskaya and the Sardakhsko-Trofimovskaya system. However, it is not entirely sure what portion of the sediment load is actually exported into the Laptev Sea.

The Bykovskaya channel drains into the Buor-Khaya Bay, which is located east of the delta in the southeastern part of the Laptev Sea and is bordered by Cape Buor-Khaya to the west (Figure 2). Its coastline is largely composed of the Yedoma ice complex, ice and carbon rich permafrost deposits that originate from the Pleistocene (Schirrmeister et al., 2011; Zimov et al., 2006) and may be especially vulnerable to the effects of climate change (Strauss et al., 2017).
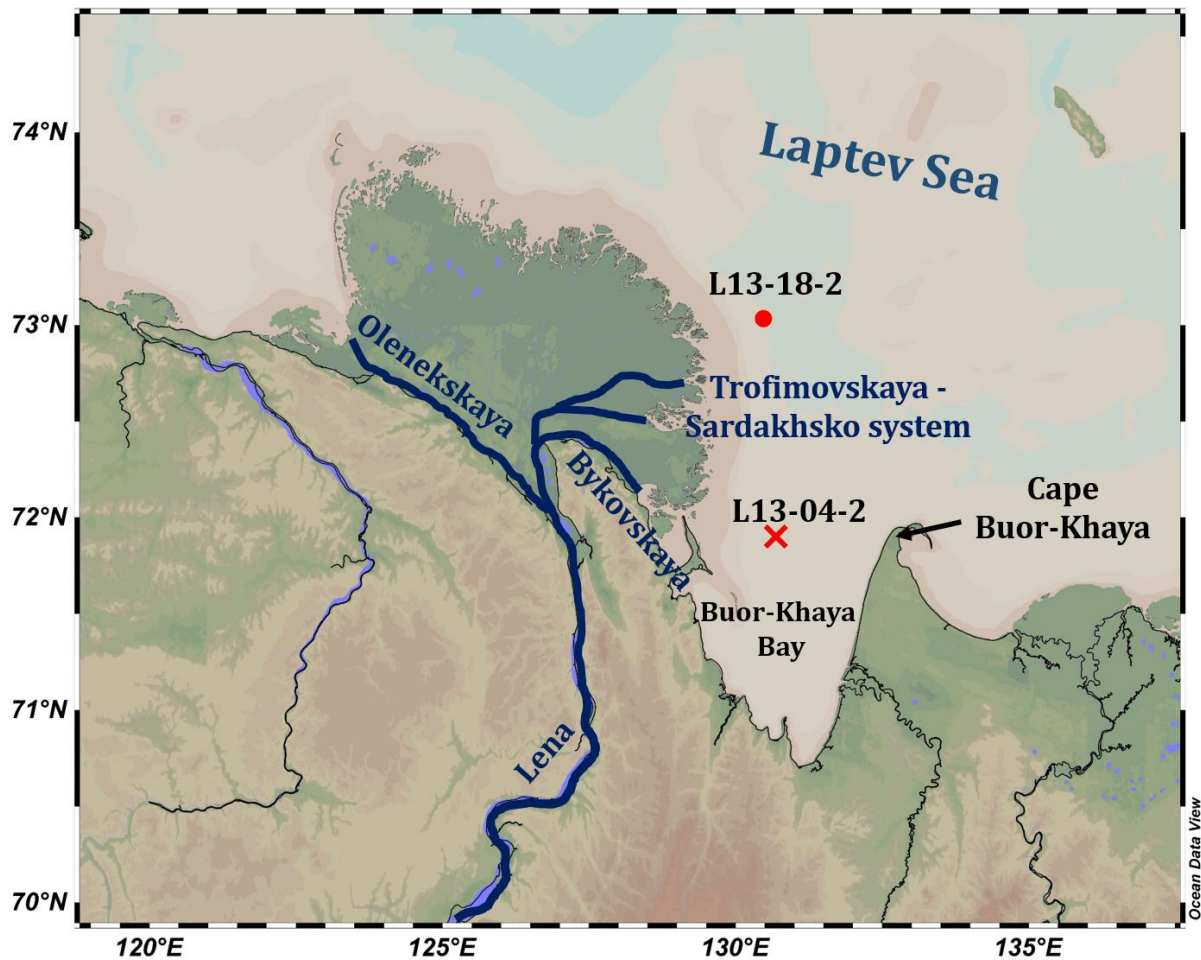
Figure 2: Map of the study area, showing the Lena delta with the three main channels, the Buor-Khaya Bay and the two core locations.

Their exposed position as steep cliffs around the bay make them susceptible to climatic influences, such as air temperature changes or erosion through wave impact. Since the formations are stabilized by the contained characteristic large ice wedges, they are prone to thermal collapse as a result of global warming. There is ample evidence for the large scale erosion in the study area, i.e. the island erosion of Moustakh Island (Günther et al., 2013; Vonk et al., 2012).

Terrestrial organic carbon in the sediments of the Laptev Sea comprises in parts of carbon derived from ice complex deposit permafrost (ICD-PF) and of carbon derived from the topsoil permafrost (TS-PF) that is of younger age and comprises the active layer.

The river and the delta are characterized by an extremely episodic flow regime, as the Lena remains almost completely frozen for 6-7 month of the year and water discharge decreases to a minimum during winter. In April, the ice break-up begins, followed by the main discharge during the spring flood in June (Figure 13).
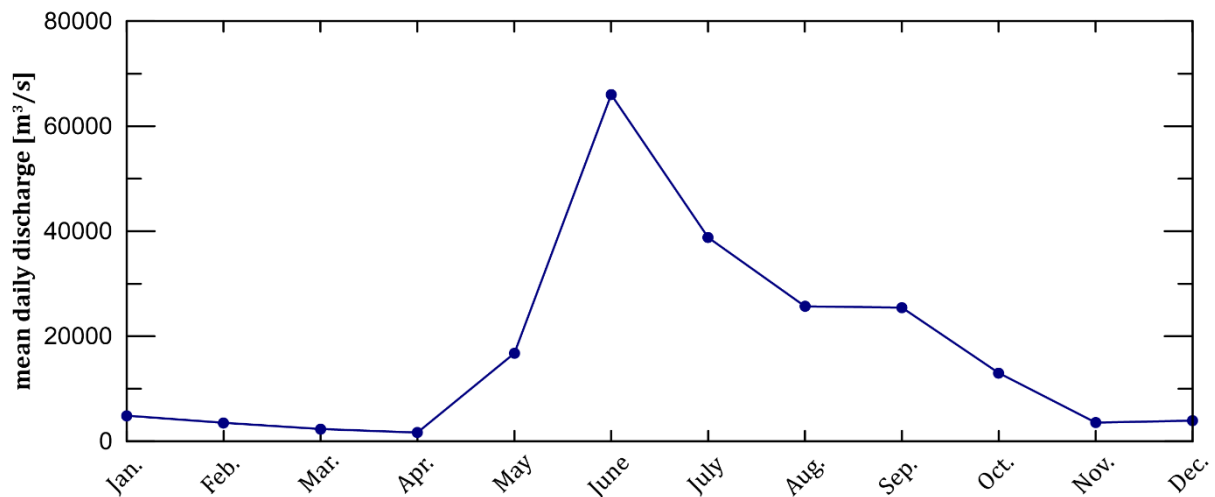
Figure 3: Water discharge profile of the Lena river in the year 2012 (ArcticGRO Discharge Dataset, www.arcticgreatrivers. org, retrieved 10 April 2018).

The catchment area is almost entirely underlain by permafrost, which has an average thickness of 100-800 m but can reach depths of up to 1500 m (Anisimov & Reneva, 2006).

Ice break-up and extensive flooding along with climate change induced instability result in the extensive erosion of the Lena delta and the adjacent coastline (Vonk et al., 2012). Ice complex deposit permafrost (ICD-PF) outcropping along the Buor-Khaya Bay is therefore prone to thermal or mechanical collapse, possibly resulting in the export of large amounts of extremely old carbon into the Laptev Sea.

Not only the geological setting, but also the vast permafrost catchment area and the immense contribution of water and sediment to the Arctic Ocean make the Lena River and its delta the ideal research subject to understand the effects of climate change on the Arctic permafrost and the export of organic matter into the Arctic Ocean.

1.3 Scientific background and objective of the study

Compound specific analysis

The isotopic composition of organic matter is determined by the composition of the carbon and hydrogen source and organism specific fractionation patterns (J M Hayes, 1993). Sediments often comprise organic material from heterogeneous unknown sources, hence deducing source related information from bulk geochemical measurements can be complicated and deceptive. Therefore, compound specific analysis of both stable and radiogenic isotopes is a powerful tool to identify individual sources of heterogeneous organic matter as well as environmental changes reflected in isotope ratio variations.

_n_-alkanoic acids as biomarkers

_n_-alkanoic acids (fatty acids) are a main constituent of membrane lipids of bacteria and eukarya and are widely used as biomarkers to trace different source organisms of organic matter in marine and terrestrial sediments. Due to their abundance _n_-alkanoic acids are not uniquely source specific, but different organism show distinct and characteristic _n_-alkanoic acid compositions. Therefore, individual or grouped _n_-alkanoic acids can be used to determine dominant sources. Although short-chain _n_-alkanoic acids, such as $C_{12:0}$, $C_{14:0}$ or $C_{16:0}$ _n_-alkanoic acids are produced by all plants, they are prevalent in algae (Cranwell et al., 1987) and used as biomarkers for primary production. In contrast, long-chain _n_-alkanoic acids, such as $C_{28:0}$ are major components in the epicuticular waxes of higher plants (land plants) (Eglinton & Hamilton, 1967; Rieley et al., 1991).

Numerous studies used _n_-alkanoic acids for source appointment or characterization of organic matter in the sediments of the Lena Delta and the Laptev Sea. Vonk et al., (2014) used radiocarbon dating of combined long-chain _n_-alkanoic acids to describe the different special distribution patterns of organic matter derived from different permafrost pools. A similar approach was used by Bröder et al. (2018), who determined cross shelf transport times of terrestrial biomarkers in the Laptev Sea. Karlsson et al. (2011) investigated the different contributions of surface soil and Yedoma permafrost to the sediments in the Buor-Khaya Bay using the stable carbon isotope ratio for differentiation. Recently, Vonk et al. (2017) suggested the compound specific stable hydrogen isotope ratio of long-chain _n_-alkanoic acids and _n_-alkanes as a tool to distinguish between the contribution of different permafrost pools to arctic sediment.

Objective of the study

Although there is great interest in the changes of contribution and distribution of permafrost derived organic matter in the Buor-Khaya Bay, most studies focus on the investigation of surface sediments. Little is known about how the effects of warming in the Arctic and the progressing thaw of permafrost are reflected in the sediment over a longer period.

This study aims to investigate how the progress of permafrost destabilization as a result of climate change is reflected in two centennial sediment records. Compound specific analyses of stable and radiogenic isotopes are used to trace variations in the sources contributing organic matter to the Buor-Khaya Bay.

2   Material and methods

2.1   Sampling and core locations

Two short sediment cores were recovered during an expedition conducted in 2013. The cores were taken about 30 km off the mouths of two main channels of the Lena River (Figure 2). Both core sites are located east of the delta in the adjacent Laptev Sea. L13-18-2, which was taken off the mouth of the Trofimovskaya channel is a 24 cm long core covering the last 80 years of sedimentation. Upon retrieval it was sampled every 1 cm down-core. L13-04-2, which was recovered in the Buor-Khaya Bay, off the mouth of the Bykovskaya channel is of 25 cm length and covers the last 150 years. It was sampled at the surface (0-1cm) and downcore from there every 2 cm. All samples were put into pre-combusted glass jars and stored frozen at -20 °C until analysis.

2.2   Bulk sediment parameters

All bulk parameter determinations were previously conducted by different scientists. The content of total carbon (TC) and total organic carbon (TOC) were measured at the Alfred Wegener Institute, Helmholtz Centre for Polar and Marine Research (AWI) in Bremerhaven (Winterfeld, 2016; unpublished). Measurements for the Constant Rate of Supply (CRS) age models with the according mass accumulation rates were conducted at the University of Bremen (Pittauer, 2018; unpublished). These additional data can be found in the appendix (Appendix Tables AT2-3; AT8-9).

2.3   Sample processing

The extraction and quantification of all lipid biomarkers as well as the compound specific radio carbon dating were conducted at the laboratory facilities of Prof. Dr. Gesine Mollenhauer at the AWI. Isotope ratio mass spectrometry measurements were performed in the laboratories of Dr. Enno Schefuß at the MARUM - Center for Marine Environmental Sciences in Bremen. Figure 4 shows a flow chart of the main work steps that were performed until analysis. Those steps are described in the following.
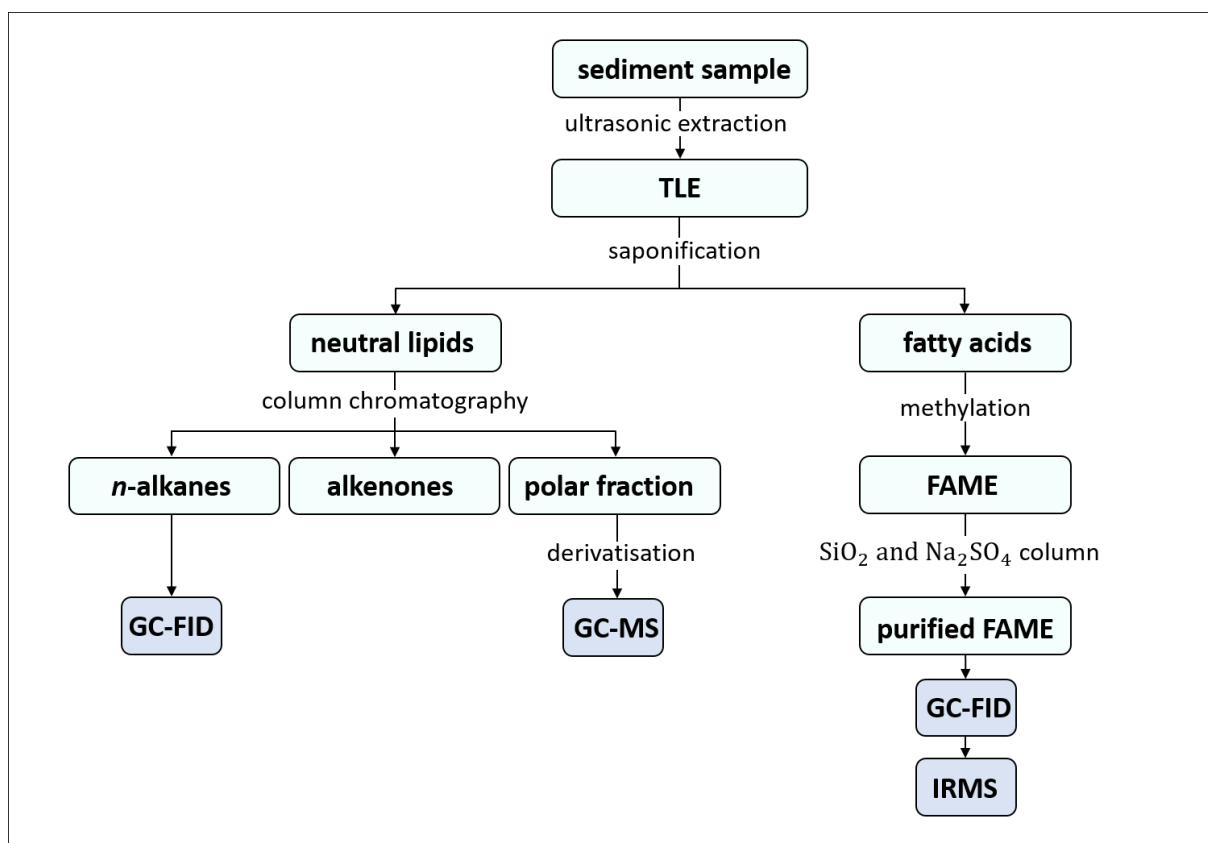
Figure 4: Flow chart of the main steps of laboratory work together with the products of each step and the analytical methods applied. Measurement methods are shown in blue boxes.

Extraction

Organic compounds were extracted from ~ 3 g of sediment using ultrasonic extraction. For quantification 100 µl of internal standard, comprising the compounds listed in Table 1 were added to each sample.

compound	concentration [ng/µl]	target compound class
squalane	82.00	*n*-alkanes
2-nonadecanone	78.68	alkenones
19-methylarachidic acid	161.04	*n*-alkanoic acids
androstanol	82.00	sterols
C46-GDGT	80.96	GDGTs

Table 1: Different compounds and their concentrations used in the internal standard along with the targeted compound class in the samples.

25 ml of a dichloromethane (DCM) and methanol (MeOH) solvent mixture in the volumetric ratio of 9:1 were added to each sediment sample. The suspension was placed in an ultrasonic bath for 10 minutes and subsequently centrifuged for 5 min at 2200 rpm. Then the supernatant solvent was decanted into a round bottom flask. Each sediment sample was extracted three consecutive times, resulting in a 75 ml total lipid extract (TLE). The TLEs were reduced to ~2 ml by roto-evaporation and filtered over glass wool and Na_2SO_4 to remove any remnant particles and remaining water. After filtration, the TLEs were dried completely under a gentle stream of N_2 at 40 °C.

Saponification

In natural samples and thus in the TLE, alkanoic acids (fatty acids) are attached to glycerol backbones via ester bounds. Saponification with KOH is used to break the ester bonds by basic hydrolysis and create free fatty acids. After the reaction, the solution contains apolar components, such as *n*-alkanes, alkenones and long chained alcohols (compiled in the term neutral lipids) as well as dissolved fatty acid potassium salts.

For saponification 1.5 ml of a 0.1 M KOH in 9:1 (v:v) H_2O and MeOH solution was added to each TLE. The glass vials containing the TLE and the KOH were then sealed and heated for 2 hours at 80 °C. In order to separate the neutral lipids (NLs), 1 ml of hexane (HEX) was added to the solution, which was then shaken to dissolve the NLs in the HEX. Then the supernatant HEX phase was removed with a pipette and the process was repeated two more times. To stabilize the free fatty acids 30 μl of a 37% HCL solution were added to the remaining saponified TLE. To extract the fatty acids, 1 ml of DCM was added, along with 1 ml of H_2O extracted with DCM for a better phase separation. By shaking the sample, the fatty acids dissolved in the DCM phase, which was subsequently removed with a pipette. That procedure was conducted three times.

After separation, both fractions were dried completely under a gentle stream of N_2 at 40 °C.

Methylation

Fatty acids are commonly analyzed as fatty acid methyl esters (FAMEs) to reduce the polarity and increase the volatility, thus allowing the measurement on non-polar GC columns. During methylation the proton of the carboxyl group is replaced with a methyl group, reducing the polarity of the functional group.

For methylation 2 ml of MeOH with a known isotopic composition were added to each dried fatty acid fraction, therefore allowing later isotopic analysis of the FAMEs. Three drops of 37 % HCl were added as an acid catalyst. To avoid a reaction with O_2, the gaseous phase inside the vial was replaced with N_2.

The samples were heated at 50 °C overnight. Extraction of the FAMEs was then performed by shaking out the samples three consecutive times with 1 ml of HEX. To remove any remnant water the FAME fraction was cleaned and purified on a column consisting of silica gel and Na_2SO_4. 4 ml of a solvent mixture of DCM:HEX 2:1 (v:v) were used to flush the sample over the column.

The cleaned FAME fraction was caught in a 4 ml vial. Any recalcitrant leftover components were removed from the column using a solvent mixture of DCM:MeOH 1:1 (v:v) and caught in a separate vial. After separation the cleaned FAME fraction was dried completely and subsequently transferred into 2 ml vials for analysis, while the DCM:MeOH fraction was not further studied.

Column chromatography of neutral lipids

Column chromatography is used to separate the neutral lipids into three different component fractions. Target compound classes are separated based on their polarity and the resulting interaction with the stationary phase. Higher polarity of a component results in stronger interaction with the stationary phase and therefore a solvent of higher polarity is required to move this component. Separation of the components is achieved by a gradual increase of solvent polarity.

For analysis the NLs were separated into alkanes, alkenones and a fraction containing polar components such as GDGTs and alcohols. Column chromatography was performed using glass pipette columns with pre-combusted deactivated SiO_2 in HEX as the stationary phase. The dried NL fraction was dissolved in 0.5 ml of HEX and transferred onto the column. Alkanes were eluted with HEX, alkenones with a mixture of DCM:HEX 2:1 (v:v) and the polar fraction with a mixture of DCM:MeOH 1:1 (v:v). Each fraction was eluted in 4 ml of the respective solvent, collected in 4 ml vials and subsequently dried. After separation the *n*-alkanes and alkenones were transferred into 2 ml vials with glass inlets for GC-FID analysis. In order to quantify polar components on the HPLC the fraction was dissolved in HEX:IPA 99:1 (v:v) and filtered through 0.45 µm PTFE syringe filters to remove any particles, before it was transferred into 2 ml vials with glass inlets.

Derivatization

In order to analyze the polar fraction on the GC-MS, it is necessary to increase volatility by decreasing the interaction with the stationary phase, thus enabling the components to elute from the column. During derivatization with N,O-Bis(trimethylsilyl)trifluoroacetamide (BTSFA) the proton in the hydroxy group is exchanged for a trimethylsilyl group of the BTSFA, producing a less polar trimethylsilyl-derivate.

For derivatization 30 µl of BTFSA and 30 µl of acetonitrile were added to the dried polar fraction and the solution was heated to 60 °C for 1h and analyzed within 24h.

Radiocarbon samples

Compound specific radiocarbon analysis (CSRA) was performed on samples, which were previously extracted using the Soxhlet method. For this method, greater amounts (20-100 g) of sediment are required, so that samples of different depths had to be combined for extraction. The surface samples of both cores were extracted separately while the combined samples cover 2-4 consecutive core cm each. In total 5 samples from core L13-04-2 and 4 samples from core L13-18-2 were extracted. Details of the samples (combined depths and CRS model age) are shown in Table 2. FAMEs of these samples had previously been separated according to chain length using preparative gas chromatography (Prep-GC). Due to their natural higher abundance FAMEs with even carbon numbers between 16 and 30 were collected for analysis.

	combined depths	mean depth	CRS age range	mean age
	0-1cm	0.5 cm	2012	2012
	4-7cm	5.5 cm	1999-1990	1994
L13-04-2	12-15cm	13.5 cm	1953-1929	1943
	17-20cm	18.5 cm	1907-1897	1902
	21-23 cm	22 cm	1888-1880	1884
	0-1cm	0.5 cm	-	2012
	5-9cm	7 cm	1997-1991	1994
L13-18-2	13-17cm	15 cm	1970-1964	1967
	21-25cm	23 cm	1942-1933	1937

Table 2: Combined sample depths for radiocarbon analysis with CRS model age range (round to full years). The stated years are the years of sediment deposition. The mean age includes all individual CRS ages of the combined depths. Individual CRS ages can be found in the appendix (Appendix Tables AE8 and AE9).

2.4 Measurement methods

2.4.1 Radiocarbon samples

AMS

Accelerator mass spectrometry (AMS) is used to detect the ratio of a long-lived radiogenic isotope to a stable isotope of the same element by accelerating ions to extraordinarily high kinetic energies before separating them according to their masses. The method completely suppresses atomic and molecular isobars, thereby creating an exceptional abundance sensitivity compared to other mass spectrometry methods. This suppression enables the reliable detection of extremely rare radionuclides within abundant stable isotopes, while requiring only small samples sizes. The main application of AMS is the measurement of ^{14}C for radiocarbon dating.

Samples are converted into CO_2 and subsequently graphitized, before they are pressed into a target. Through a vacuum lock, the target is inserted into a sputter ion source, in which an ion beam (usually Cs^+) is accelerated onto the target and sputter negatively charged carbon ions out of the sample. Negative ionization is used to dispose of the isobar ^{14}N, which cannot produce anions. The resulting potential difference accelerates the negatively charged ions away from the target and into a focusing device. The focused ion beam is deflected orthogonally by an injector magnet to separate the individual ions according to their mass and to remove all non-carbon-ions. Ions of selected masses move into a tandem accelerator unit, where ions are first accelerated to a high positive potential and subsequently pass through an electron stripper. In this step all remaining molecules are scattered into molecule fragments and carbon ions. The emerging carbon ions are accelerated and introduced into a second magnet that separates the beam according to mass by deflection, thereby removing any remnant molecule fragments. Finally, the selected ions are detected by measuring the amperage of the individual beam using a Faraday cup.

Measurements were conducted using the *MIni CArbon DAting System* (MICADAS 15), produced by Ionplus AG. Besides the analysis of graphitized samples, the MICADAS allows the measurement of gaseous samples by an optimized ion source. Due to this feature, reliable results can be achieved for measurements of samples as small as 10 μgC. The FAME samples were dissolved in DCM and transferred into small tin cups. After the solvent was evaporated, the tin cups were folded and combusted using a *vario ISOTOPE select Elemental Analyzer* (EA), which was connected to the MICADAS via a Gas Ion Source Interface (GIS) produced by Ionplus AG. The CO_2 generated in the EA is transferred onto a zeolite trap inside the GIS, which was operated at 28 °C. The amount of carbon in a sample is calculated according to the to the CO_2 gas pressure by a pressure sensor inside the GIS. After the CO_2 was adsorbed onto the trap, the temperature was abruptly increased to 450 °C, releasing the sample gas into a syringe, which introduces the gas into the ion source of the MICADAS. Specific settings of the machine can be found in Synal et al. (2007).

The samples were measured in order of deposition of the sediment (from old to young) to avoid radiocarbon cross contamination. CSRA results are reported as fraction Modern Carbon (*fMC*), which is calculated as follows (Stuiver & Polach, 1977):

$$fMC = \frac{^{14}C/^{12}C_{sample}}{^{14}C/^{12}C_{standard}} \tag{1}$$

The $^{14}C/^{12}C_{standard}$ ratio is defined to equal the pre-Bomb-Pulse atmospheric composition.

2.4.2 Lipid biomarker samples

GC

Gas chromatography (GC) is an analytical method to separate a mixture of gaseous analytes according to their boiling point and the interaction with a solid stationary phase. It is applicable to any gaseous sample or samples that can be vaporized without structural decomposition. Apolar analytes (*n*-alkanes) and analytes with a low to intermediate polarity (alkenones) can be separated. A split/splitless-injector is used to rapidly vaporize the sample if necessary and inject it onto the separation column. The column is located in a temperature-controlled oven and consists of a rolled-up capillary lined with a polymer, which acts as the stationary phase. Upon injection, the sample condenses at the start of the column, before the temperature is gradually increased to evaporate the components successively. An inert gas is used as a mobile phase and carries the analytes over the column, where they are repeatedly adsorbed onto the stationary phase and eluted by the carrier gas. According to their boiling point, vapor pressure and molecule size the resulting flow rate varies for each analyte, thus separating the individual compounds. Increased molecule size, a high boiling point and low vapor pressure result in slower elution. The separation quality is proportional to count of adsorption steps and expressed through the number of theoretical plates of a separation column. A detector at the end of the column determines the time of exit (retention time) of each eluent.

GC-FID

Gas chromatographs can be coupled to different analytical devices, i.e. a flame ionization detector. This method is used to quantify oxidizable components separated by GC and is connected directly to the separation column. Under an influx of hydrogen and air, the analytes are carried into a positively charged hydrogen flame, including a reduction zone. The compounds are burned, first producing $CH^{\cdot}$, which are oxidized to CHO^{+} ions and electrons. A cylindrical cathode around the flame applies an electrical potential and collects the electrons. The signal of the incoming electrons

is directly proportional to the amount of burned analyte. It is measured as an electric current and recorded as a peak with the respective retention time. Quantification of each analyte is conducted by peak area integration, relative to the peak size of an internal STD with known concentration. Analysis was performed on an *Agilent 7890A GC system*, equipped with a 60 m DB-5 (Agilent J&W GC Products; 250 µm internal diameter, 0.25 µm film thickness) separation column. 1 µl of sample was injected as a liquid on-column-injection by an *Agilent 7693 autosampler*. The initial temperature of 60 °C was held for 1 min, then increased to 150 °C via a 20 °C/min gradient and subsequently raised with a gradient of 6 °C/min to 320 °C, which was held for 35 min. The detector was operated at 330 °C.

GC-MS

Mass spectrometry is a tool to obtain information about the molecular structure and mass of unknown organic compounds. There are various types of MS, but operation is based on the same principle and they are usually coupled to a chromatographic device, i.e. a GC. Separated compounds are directed into the MS, where they are ionized and to different extends fragmented. Fragmentation occurs in a component-specific matter, producing characteristic mass fragments for the individual analytes. The ionized molecular fragments are accelerated in an electric or magnetic field that separates them according to their mass/charge (m/z) ratio by deflecting their flight paths. A detector converts the signal of incoming ions into an electric current, which is displayed as a peak. Components can be identified using their characteristic fragment patterns and peak area integration is used for semi-quantification. The detector can be set to scan in acquisition mode (broad range of mass fragments) or single ion mode (specific mass fragments). Analysis was performed on an *Agilent 6850 GC system*, equipped with a 30 m DB-1 separation column (Restek, Rxi-1ms; 0.25 mm inner diameter, 0.25 µm film thickness) and operated in 1.2 ml/min constant flow modus. 1 µl of sample were vaporized at 280 °C and injected in splitless mode. Upon injection the sample was focused for 3 min at 60 °C before the temperature was increased to 150 °C via a 20 °C/min gradient, followed by a 4 °C/min increase to 320 °C. The final temperature was held for 15 min. Mass spectrometry was conducted using an *Agilent Technologies 5975C VL MSD* in acquisition mode (50-600 amu), with ionization energy set to 70 eV.

2.4.3 Isotope ratio measurements

IRMS

Isotope ratio mass spectrometry (IRMS) is a method used to determine the relative ratio of the stable isotopes of light elements, i.e. of carbon ($\delta^{13}C = {}^{13}C/{}^{12}C$) or hydrogen ($\delta^2H = {}^2H/{}^1H$). Prior to analysis, the sample is separated using GC. For carbon isotope analysis the individual eluents are transferred into an oxidation combustion reactor, an aluminum or ceramic tube containing metal wire catalyzers. At temperatures around 950 °C the analyte is combusted to CO_2 and H_2O, which is removed by diffusion through a semi-permeable Nafion membrane.

For δ^2H analysis, eluents are not combusted, but directed into a pyrolysis reactor operated at ~1400 °C which converts the analyte into CO, C and H_2. The analyte gas is moved by an inert carrier gas into the ion source, where it is ionized by electron ionization at 150 eV, producing ions of different masses. In carbon analysis, three CO_2 isotopologues are produced: ${}^{12}C^{16}O^{16}O$ (m/z = 44), ${}^{13}C^{16}O^{16}O$ (m/z = 45) and ${}^{13}C^{16}O^{18}O$ (m/z = 46). Ionization of hydrogen isotope samples produces the isotopologues: ${}^1H^1H$ (m/z = 2) and ${}^2H^1H$ (m/z = 3). The ion beam passes through a beam focuser into a magnetic sector that separates individual ions according to their m/z ratio by deflecting their flight paths. Individual ions with the same m/z ratio are detected using Faraday cups as they induce an electric current proportional to the number of incoming ions. The signal is then converted into peaks. Stable isotope ratios are determined by relating the integrated peak area to peak areas of reference CO_2 gas. The reference gas is calibrated against the Vienna Pee Dee Belemnite (VPDB) standard for $\delta^{13}C$ and against the Vienna Standard Mean Ocean Water (VS-MOW) standard for δ^2H analysis. Results are expressed in the dimensionless 'per mille' notation.

Carbon isotope measurement was conducted using a *Finnigan MAT 252* isotope ratio mass spectrometer, connected to a *Thermo Scientific Trace GC Ultra* gas chromatograph fitted with a 30 m DB-5 separation column (Restek, Rxi-5ms; 0.25 mm inner diameter, 0.25 μm film thickness). The temperature program of the GC was set to 120 °C for 3 min at the start, followed by a 5 °C/min gradient until 320 °C, which was held for 17 min.

Hydrogen isotopes were measured with a *Thermo Finnigan MAT 253* mass spectrometer, connected to a *Thermo Scientific Trace GC Ultra* gas chromatograph fitted with a 30 m DB-5 separation column (Agilent J&W GC Products; 250 μm internal diameter, 1 μm film thickness). The temperature was set to 120 °C for 3 min, increased by a 30 °C/min ramp to 200 °C, followed by a 4 °C/min gradient to 320 °C, which were held for 25 min.

2.5 Complementary calculations

2.5.1 Blank and methyl corrections

Methylation of *n*-alkanoic acids results in the incorporation of a methyl group that was not originally present in the molecule and therefore distorts any information based on carbon or hydrogen isotope analysis. In order to determine the correct isotope ratios for the *n*-alkanoic acids, results of IRMS and CSRA have to be methyl corrected. For this reason, MeOH with a known isotopic composition (shown in Table 2) was used for methylation.

	MeOH 1	MeOH 2	MeOH 3
$\delta^{13}C$ [‰]	-28.3 ± 0.50	-29.1 ± 0.48	-
δ^2H [‰]	-156 ± 2.0	-133.7 ± 3.1	-
fMC	-	-	0.0008 ± 0.0001

Table 3: Isotopic compositions of the different MeOH charges used for methylation. MeOH 3 was used for the fatty acids of the Soxhlet-extracted samples, which were set to be radiocarbon dated. Therefore, only the fMC of MeOH 3 was determined.

Stable isotope ratio correction

The following mass balance equation is used to show the composition of the $\delta^{13}C$ results, where $\delta^{13}C_m$ is the measured value from IRMS, $\delta^{13}C_{MeOH}$ is the $^{13}C/^{12}C$ ratio of the used MeOH, $\delta^{13}C_{smp}$ is the correct isotopic ratio of the sample and *n* is the total number of carbon atoms after methylation:

$$\delta^{13}C_m = \frac{1}{n} * \delta^{13}C_{MeOH} + \frac{n-1}{n} * \delta^{13}C_{smp} \tag{2}$$

Equation (2) can be rearranged to calculate $\delta^{13}C_{smp}$:

$$\delta^{13}C_{smp} = \left(\delta^{13}C_m - \frac{1}{n} * \delta^{13}C_{MeOH}\right) * \frac{n}{n-1}$$

The same approach can be used to determine the correct δD value of a sample (δD_{smp}), in this equation *n* is the total number of hydrogen atoms after methylation:

$$\delta^2 H_m = \frac{3}{n} * \delta D_{MeOH} + \frac{n-3}{n} * \delta D_{smp} \tag{3}$$

Rearrangement yields:

$$\delta^2 H_{smp} = \left(\delta D_m - \frac{3}{n} * \delta D_{MeOH}\right) * \frac{n}{n-3}$$

Errors for $\delta^{13}C$ and δ^2H were calculated using error propagation (Appendix Equation AE1 and AE2).

Radiogenic isotope correction

Results of CSRA measurements are distorted not only by the co-analysis of the incorporated methyl group but also by contaminating extraneous carbon, the so-called procedural blank. Therefore, a blank correction and a methyl correction according to Hwang and Druffel (2005) were conducted on all CRSA measurement values. A detailed description including all performed steps and calculations can be found in the appendix.

2.5.2 $\Delta^{14}C_{initial}$ calculation

For discussion considering radiocarbon enrichment or depletion, fMC is converted into $\Delta^{14}C$, a term reported in the 'per mille' notation. It is necessary to correct the results for the amount of ^{14}C decayed after deposition. Therefore, $\Delta^{14}C_{initial}$ ($\Delta^{14}C$ at the time of deposition) is calculated as follows (Stuiver & Polach, 1977), where ysd are the years since deposition and $t_{0.5}$ is the half-life time of ^{14}C (5730 years):

$$\Delta^{14}C_{initial} = (fMC_{smp} * e^{\left(\frac{\ln(2)}{t_{0.5}}*ysd\right)} - 1) * 1000\ ‰ \tag{4}$$

All individual $\Delta^{14}C_{initial}$ values can be found in the appendix (Appendix Tables AT11 and AT13) along with the respective errors, calculated using error propagation.

3 Results

Measurement results can be found in the appendix (Appendix Tables AT4 – AT18). Subject of this study are saturated *n*-alkanoic acids, therefore the abbreviation $C_{n:0}$ used in the results and discussion part refers to the alkanoic acid with n defining the length of the carbon chain.

3.1 Compound specific radiocarbon analysis

It is important to note that CRSA measurements were conducted on combined samples, hence $\Delta^{14}C_{initial}$ values are a mean of the combined depths.

As shown in Figure 5 and Figure 6, $\Delta^{14}C_{initial}$ values range between -100 and -600 ‰ in core L13-04-2 (Figure 5) and between -150 and -550 ‰ in core L13-18-2 (Figure 6), equaling age ranges of around 1300-7000 and 1800-5700 years respectively. Certain trends can be observed in both cores, like a significant decrease in $\Delta^{14}C_{initial}$ values with increasing carbon chain length. Longer *n*-alkanoic acids show less variability in $\Delta^{14}C_{initial}$ than shorter ones and the only *n*-alkanoic acid with a consistent trend of decreasing $\Delta^{14}C_{initial}$ downcore is $C_{16:0}$. In both cores, a severe age drop in the $C_{18:0}$ surface sample was measured.

Except from the surface sample trends and values of $C_{18:0}$ tend to be more similar to $C_{16:0}$ in core L13-04-2 whereas they resemble longer alkanoic acids in L13-18-2. The $\Delta^{14}C_{initial}$ increase of $C_{16:0}$ is more abrupt in L13-04-2, reaching an age plateau at the core top. In contrast, the slope is rather gradual in L13-18-2.
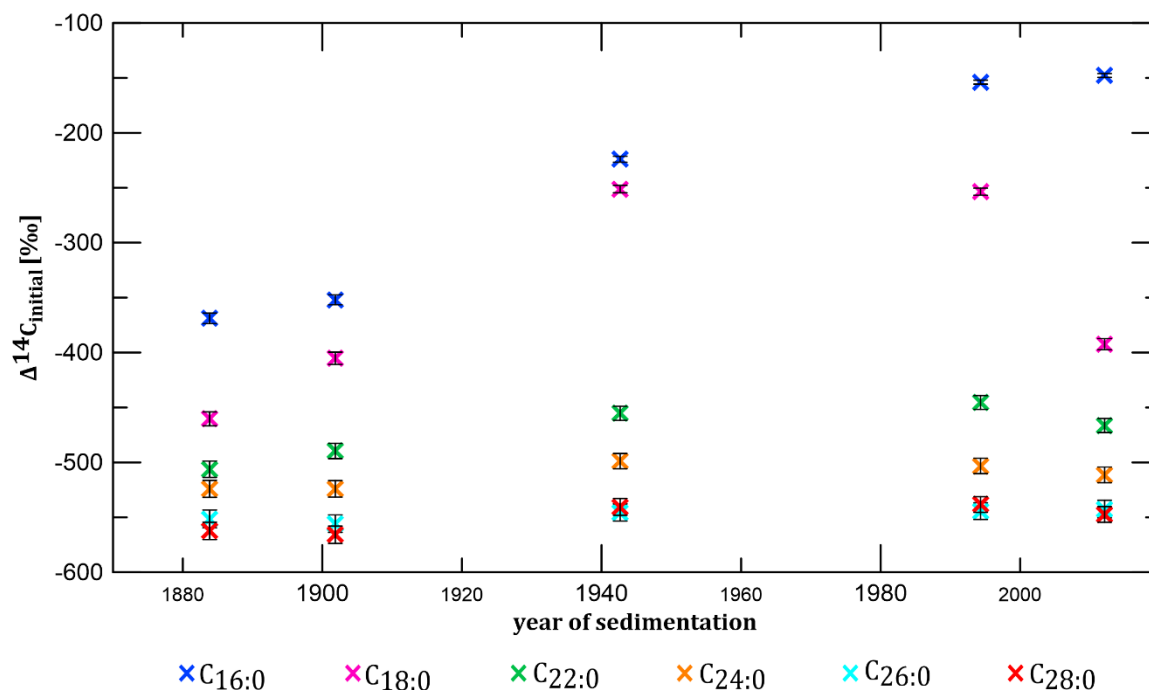
Figure 5: Radiocarbon dating results of core L13-04-2, reported as Δ14Cinitial versus year of sedimentation. Individual errors are always shown but are smaller than the symbol size in some cases.
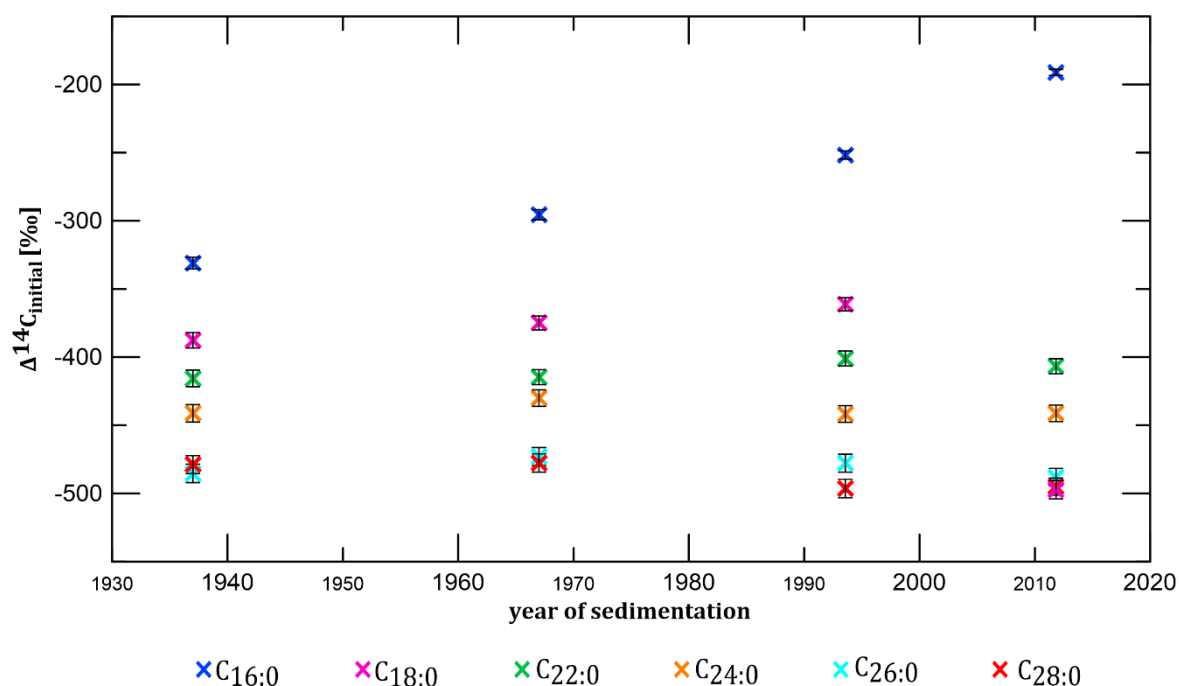
Figure 6: Radiocarbon dating results of core L13-18-2, reported as Δ14Cinitial versus year of sedimentation. Individual errors are always shown but are smaller than the symbol size in some cases.

While $C_{16:0}$ and $C_{28:0}$ alkanoic acids are thought to be of marine and terrestrial origin respectively, the sources of *n*-alkanoic acids with intermediate carbon chain length are more ambiguous. Therefore, results and their discussion are hereafter reduced to $C_{16:0}$ and $C_{28:0}$ alkanoic acids.

3.2 Concentrations and isotope ratios

As in Figure 5, Figure 7 shows $\Delta^{14}C_{initial}$ of $C_{16:0}$ and $C_{28:0}$ in core L13-04-2 plotted against the year of sedimentation in the bottom quarter. Concentrations, carbon and hydrogen isotope ratios are displayed in the remaining quarters above.

$\Delta^{14}C_{initial}$ of $C_{16:0}$ ranges between -148 ‰ and -369 ‰ and is highest in the surface sample, where the equaling age is 1327 years. Values steadily decrease to -224 ‰ over a period of about 70 years, before $\Delta^{14}C_{initial}$ decreases rapidly to -352 ‰ over a period of just 40 years. There is only a minor decline to the last sample of the core, which has an age of 3940 years. The downcore profile of $C_{28:0}$ is more constant, with $\Delta^{14}C_{initial}$ ranging from -538 ‰ to - 565 ‰ (6412 - 7030 years). From the core top, $\Delta^{14}C_{initial}$ increases slightly, is relatively constant in the middle of the core and decreases around 1940 before reaching the minimum value around 1900.

Figure 7: Results of CRSA, IRMS and concentration measurements of n-alkanoic acids C16:0 and C28:0 in core L13-04-2 plotted against the year of sedimentation. Individual errors are shown (except for concentrations) but are mostly smaller than the symbol size.

Concentration of $C_{16:0}$ is highest at the core top with 1314 µg/gTOC and decreases sharply in the underlying four samples. Higher concentrations were measured in the samples deposited between 1965 and 1985. Downcore from the year 1965 $C_{16:0}$ shows little variation and concentrations stay below 300 µg/gTOC. Concentrations of $C_{28:0}$ range from 143-291 µg/gTOC and remain almost constant throughout the core with only minor changes after 1960. In sediment deposited before 1960 concentrations of the two alkanoic acids are almost identical.

Stable carbon isotope ratios of $C_{16:0}$ exhibit a downcore profile very similar to the concentration trend and range from -21.5 ‰ to -32.5 ‰. It is most enriched in ^{13}C in the surface sample and subsequently depletes towards $\delta^{13}C$ = -31 ‰ around 1990. In the sediment deposited before 1990 there is an increase in values similar to the increased concentrations. A slight depletion can be observed downcore from the year 1950 until the minimum is reached around 1880. In contrast, constant depleted $\delta^{13}C$ values (-33 ‰) were measured for $C_{28:0}$ throughout the whole core. Marginal changes (±0.6 ‰) occur, but don't exhibit trends.

The $C_{16:0}$ hydrogen isotope ratios range from – 336 ‰ at the core top to -234 ‰ at the end. After an initial pronounced ^{2}H enrichment until 1990, $\delta^{2}H$ decreases again and subsequently increases with progressing core depth. In the sediment deposited before 1950 $\delta^{2}H$ is relatively constant. The downcore trend of $\delta^{2}H$ is exactly opposite to $\delta^{13}C$, which is especially notable in the change of values around 1980. Contrary to $C_{16:0}$, $C_{28:0}$ is most ^{2}H-enriched ($\delta^{2}H$ = -216) in the surface and values decrease downcore. At 1990 $\delta^{2}H$ is at a minimum of -239 ‰, after which it increases slightly to -229 ‰ and successively decreases with minor variations towards the end of the core. $\delta^{2}H$ values in the samples deposited before 1920 are quasi-identical in $C_{16:0}$ and $C_{28:0}$.
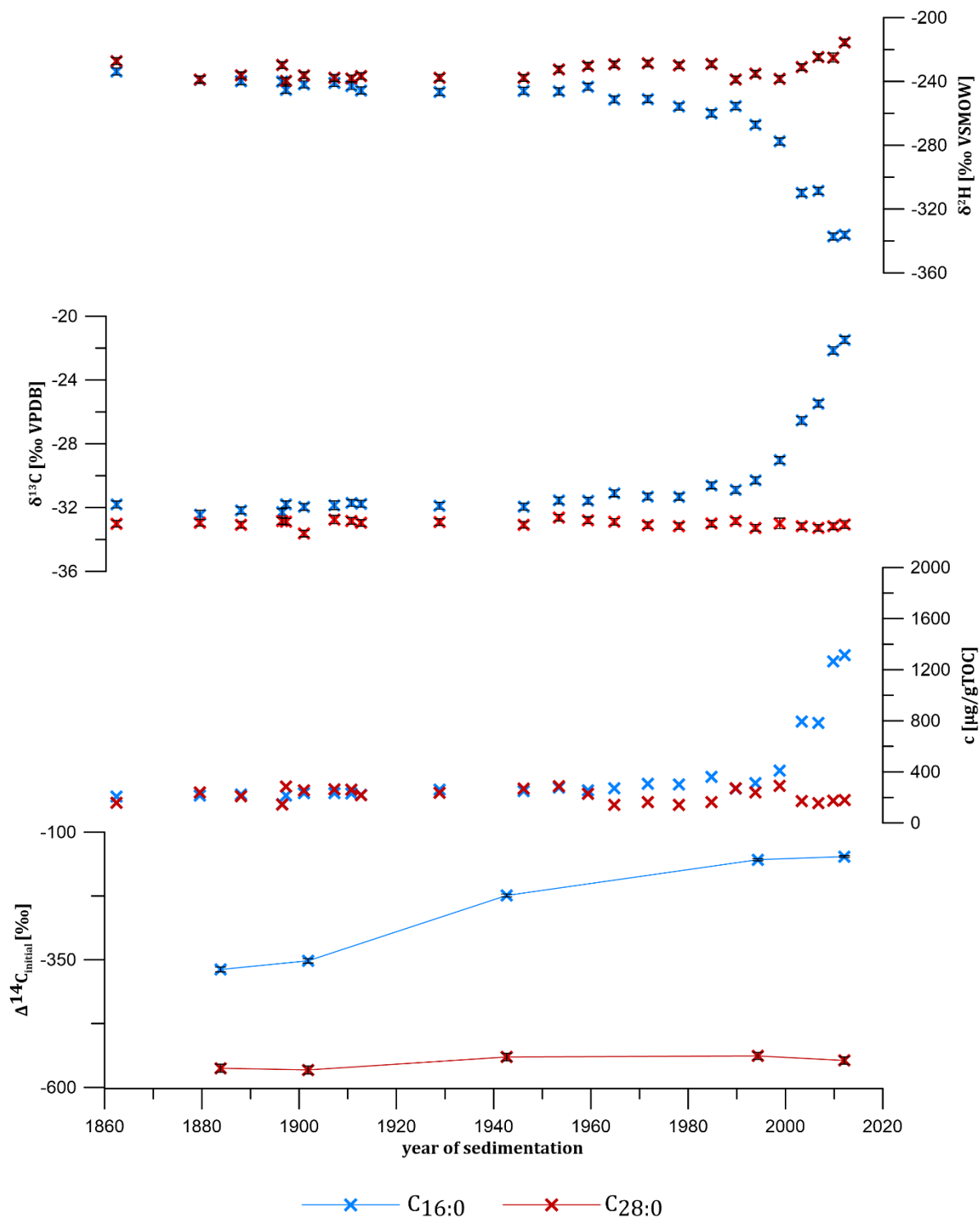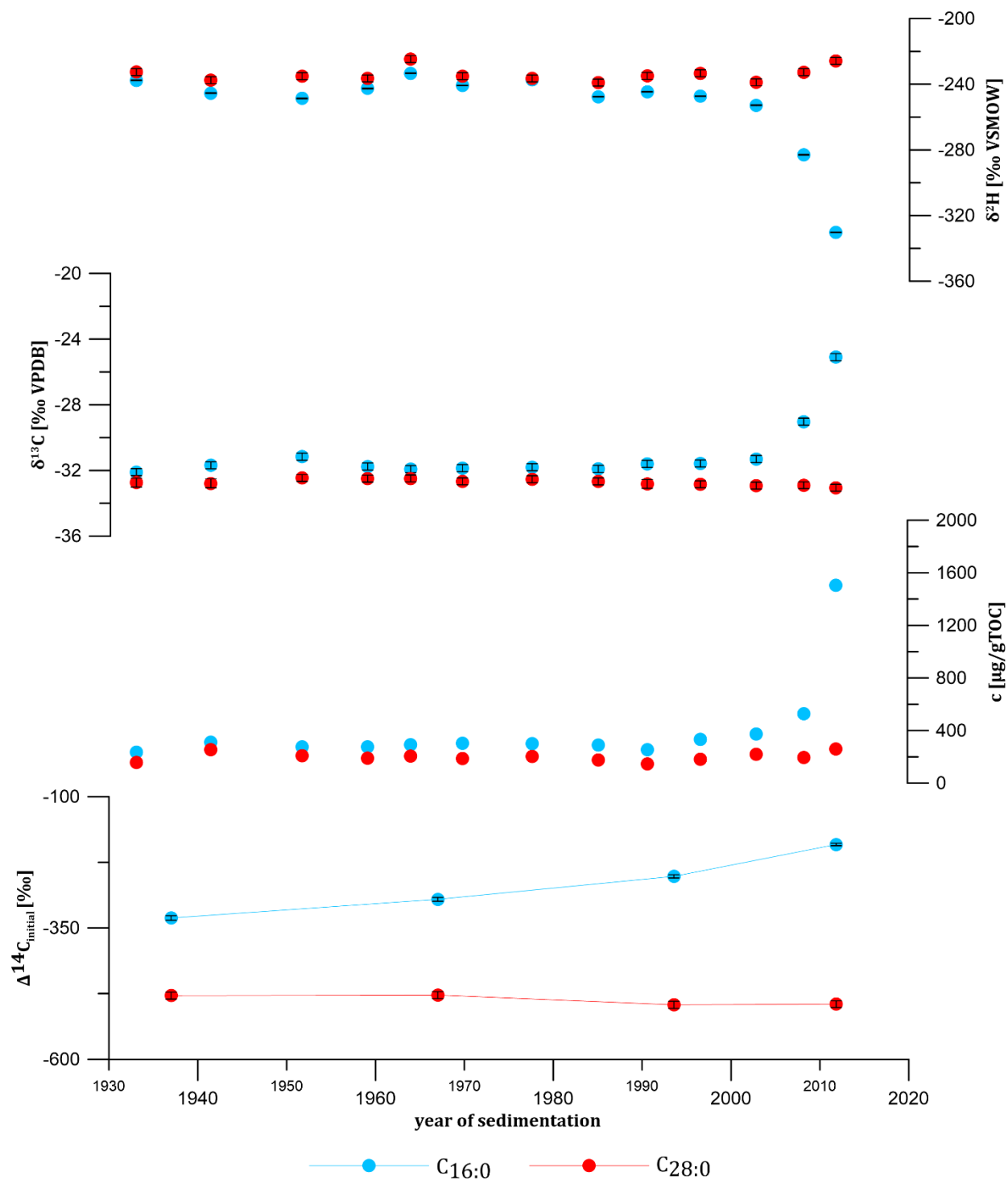
Figure 8: Results of CRSA, IRMS and concentration measurements of n-alkanoic acids C16:0 and C28:0 in core L13-18-2 plotted against the year of sedimentation. Individual errors are shown (except for concentrations) but are mostly smaller than the symbol size.

In core L13-18-2 $\Delta^{14}C_{initial}$ of $C_{16:0}$ ranges between -191 ‰ and -331 ‰, which is equal to ages between 1760 and 3399 years. The highest $\Delta^{14}C_{initial}$ was measured in the surface sample and values successively decline downcore, with decreasing differences between two neighboring samples from the top to the end of the core. In $C_{28:0}$ $\Delta^{14}C_{initial}$ values lie between -495 ‰ and -478 ‰ (5420-5695 years). $\Delta^{14}C_{initial}$ is slightly lower in the younger part of the core but there is no distinct trend visible.

Concentration of $C_{16:0}$ is highest at the core top with 1505 µg/gTOC and drops quickly in the next samples. Below the year 2000 the increasing trend subsides and there is only little fluctuation to be observed in sediment deposited before 1990. Almost all concentrations are below 300 µg/gTOC. The lowest value is reached at the bottom of the core with 234 µg/gTOC. A similar pattern can be observed in the profile of the $C_{28:0}$ concentrations that range from 147 µg/gTOC to 260 µg/gTOC. The overall trend is the same with the highest concentration at the core top, but since the difference to the downcore samples is marginal, it is difficult to distinguish between a distinct concentration increase and fluctuation around a mean.

The $\delta^{13}C$ profile of $C_{16:0}$ ranges from -25.1 ‰ in the surface sample to -32.1 ‰ at the bottom of the core. $\delta^{13}C$ decreases quickly below the core surface. Downcore from the year 2000 the pronounced decrease subsides but values continue to decrease until they remain constant in sediment deposited before 1980, with one minor increase around 1950.

 $\delta^{13}C$ values of $C_{28:0}$ are constantly between – 32 ‰ and -33 ‰ throughout the whole core.

The $C_{16:0}$ hydrogen isotope ratio exhibits a trend from strongly ^2H depleted (-330.2 ‰) values at the core top to more enriched ones (-230 to -250 ‰) in sediment deposited before the year 2000. The most enriched δ^2H was measured in the sediment deposited in 1964. Samples deposited before 2000 show only small-scale variations, with values between -224.7 to -239 ‰. It is noteworthy, that the δ^2H profile is exactly opposite to the $\delta^{13}C$ one, which is even noticeable within the small-scale variations, i.e. the small δ^2H minimum around 1950 is opposed by a maximum in $\delta^{13}C$. In sediment deposited before 2000, δ^2H follows the very same trend observed in $C_{16:0.}$ The most enriched δ^2H was also measured in the sample deposited in 1964.

Although the range and trend slope of $\Delta^{14}C_{initial}$ are different in both cores, there are similarities in the overall trends: $\Delta^{14}C_{initial}$ of $C_{16:0}$ is highest in the surface sample and decreases downcore. It is generally higher than $\Delta^{14}C_{initial}$ of $C_{28:0,}$ which remains comparatively constant. All $C_{16:0}$ samples are younger and all $C_{28:0}$ samples are older in L13-04-2 compared to L13-18-2. The same exponential decrease in $C_{16:0}$ concentrations can be seen in both cores, but it is more pronounced in L13-18-2 whereas the concentration downtrend in L13-04-2 progresses into deeper layers of the core.

There is a slight increase of $C_{28:0}$ concentration in the surface area of L13-18-2, that is not as pronounced in L13-04-2. In L13-04-2 $\delta^{13}C$ values in the surface samples are ~4 ‰ higher (more enriched) than in L13-18-2.

δ^2H ranges and trends are virtually identical in both cores, with a bit more variation downcore in L13-18-2 and slightly more enriched values of $C_{28:0}$ in L13-04-2's surface samples.

3.3 Biomarker proxies

Sterols can be used as source appointing biomarkers, due to their characteristic distribution in organisms and their resistance to degradation. The ratio of β-sitosterol, which is mainly produced by higher plants to brassicasterole and dinosterol, which are algal source markers can be used to distinguish between terrestrial and marine input (Volkman, 1986). The β-sitosterol index is calculated as follows, where c is the concentration:

$$\beta - sitosterol\ index = \frac{c_{\beta-sitosterol}}{c_{\beta-sitosterol} + c_{brassicasterol} + c_{dinosterol}} \tag{5}$$

Degradation of OM is associated with the loss of functional groups. Because perennially frozen carbon is excluded from the geochemical cycle, concentrations of lipids still incorporating functional groups (i.e. n-alkanoic acids) are a lot higher in ICD-PF compared to TS-PF. Therefore, the ratio of High Molecule Weight (HMW) n-alkanoic acids to HMW n-alkanes can be used to estimate the ratio of contributing sources to a sample:

$$HMW\ ratio = \frac{\sum_{>C22\ n-alkanoic\ acids}}{\sum_{>C21\ n-alkanes}} \tag{6}$$

Mass accumulation rates of individual lipids were calculated by multiplying the respective concentration [µg/gTOC] with the mass accumulation rate.

Additionally calculated proxies are plotted as a direct comparison of both cores (Figure 9).
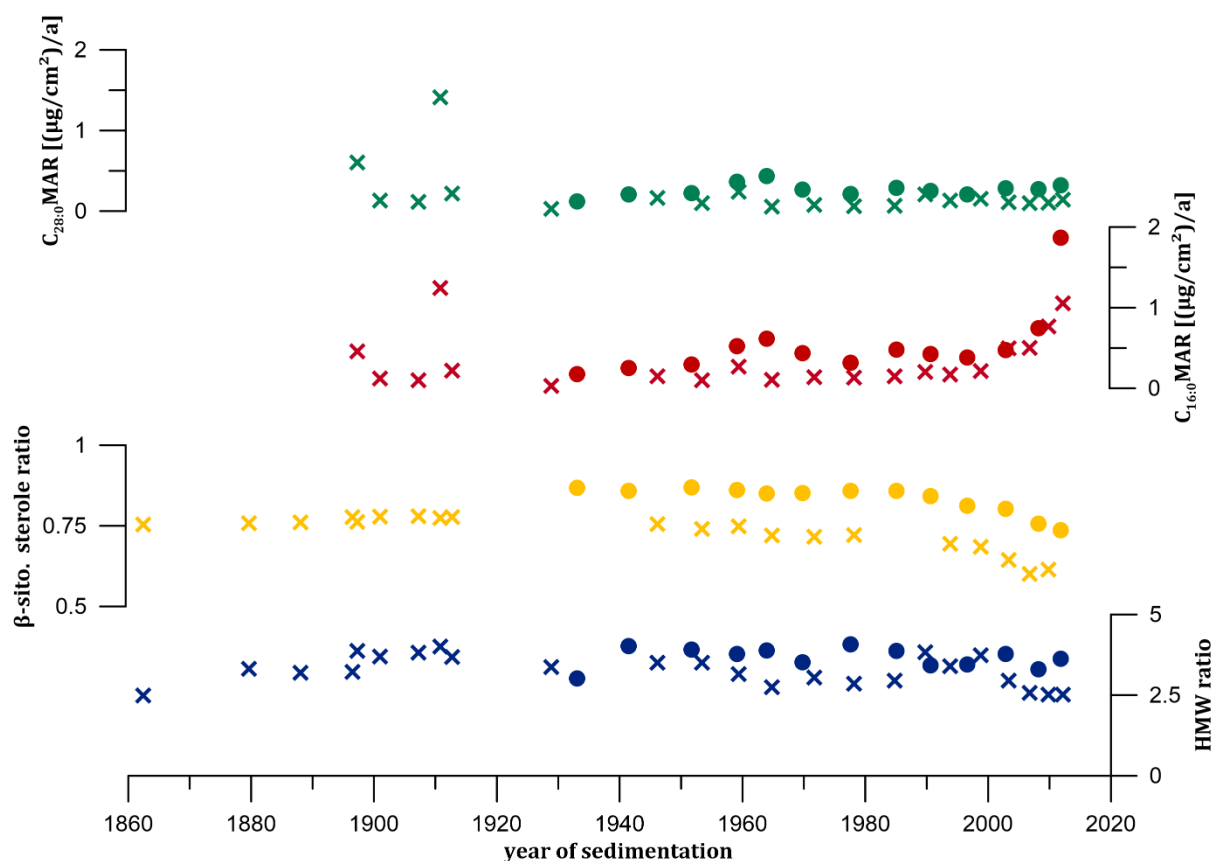
Figure 9: Additionally calculated proxies compared for both cores. Values of L13-04-2 are depicted as crosses and values of L13-18-2 as dots.

The HMW ratios of both cores fluctuate around a mean of 2.5 (L13-04-2) and 2.9 (L13-18-2). Values are a bit higher in L13-18-2 and the ratio decreases at the end of both cores. Overall, they range from 1.9-3.2 in both cores.

In L13-04-2 the β-sitosterol index could not be calculated in some samples, hence the data gaps in the profile. Ratios range from 0.61-0.78 (L13-04-2) and from 0.75-0.87 (L13-18-2). In L13-04-2 the index rises steadily with increasing core depths. It remains constant in sediment deposited before 1920. In L13-18-2 the index exhibits a more pronounced increase downcore and remains constant in sediment deposited before 1980-1990.

Mass accumulation rates of $C_{16:0}$ range between 0.03 -1.2 µg/cm^2)/a in L13-04-2 and 0.18-1.9 (µg/cm^2)/a in L13-18-2. Both cores exhibit the highest mass accumulation rate of $C_{16:0}$ in the surface samples. It decreases in the underlying sediment and is constant for the time before 2000 in L13-04-2. There are minor variations (i.e. a maximum around 1960) in L13-18-2. The maximum around 1910 is treated as an outlier value, both for $C_{16:0}$ and $C_{28:0}$. Accumulation rates of $C_{28:0}$ are generally higher (0.11-0.43 (µg/cm^2)/a) in core L13-18-2 than in L13-04-2 (0.028-0.6 (µg/cm^2)/a). The trend is the same in both cores and the accumulation rate remains constant downcore with a slight increase in the last sample.

24

A dual-carbon plot showing $\Delta^{14}C_{initial}$ versus $\delta^{13}C$ can be used to estimate the contribution of different sources (endmembers) to the isotopic composition of a sample (Figure 10).

The endmember approach is based on the assumption, that different environmental sources have characteristic bulk or molecular features, they can contribute to a sample. If these features and the number of sources are known, the proportions of sources contributing to said sample can be calculated.

Since CSRA measurements were conducted on mixed samples (Table 2), the plotted $\delta^{13}C$ is the mean value of the combined depths used for CSRA. For comparison, Figure 10 includes data points of surface bulk organic matter (OM) samples of the two cores. $\delta^{13}C$ and *fMC* of the bulk samples were previously measured (Han, 2014). For this study, *fMC* was converted into $\Delta^{14}C_{initial}$.
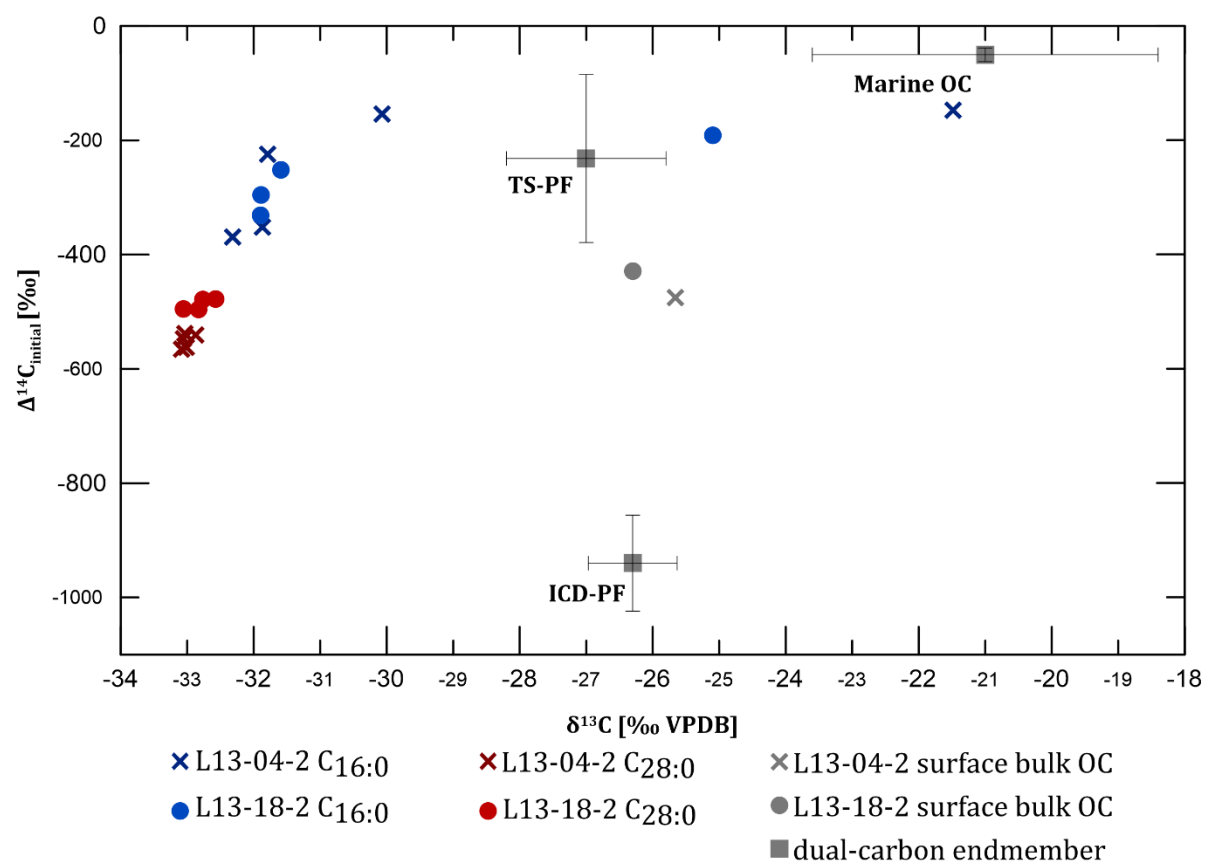
Figure 10: Dual-carbon plot of measured samples (colored) and previously analyzed bulk OC samples (grey) from the surfaces of both cores (Han, 2014; unpublished). Endmember values are taken from (Vonk et al., 2017 and references therein). Note that the endmember values are calculated as $\Delta^{14}C$ resulting in an estimated offset of +7 ‰ compared to the samples.

As $C_{16:0}$ exhibits decreasing $\delta^{13}C$ values in both cores (Figure 7 and Figure 8), their distribution on the $\delta^{13}C$ scale represents a downcore profile (from right to left on the x-axis). The surface samples of both cores lie within the marine OC $\delta^{13}C$ range (L13-04-2) and between the marine OC and TS-PF endmember (L13-18-2). There is a massive decrease in $\delta^{13}C$ from the first to the second sample

25

in L13-04-2 and another smaller step of depletion from there to the other $C_{16:0}$ samples.Further downcore the majority of $C_{16:0}$ samples concentrate in an area of strongly depleted $\delta^{13}C$ outside the defined endmember ranges. All $C_{16:0}$ samples lie within the $\Delta^{14}C_{initial}$ TS-PF range. With increasing core depths and thus with increasing time since deposition, $C_{16:0}$ samples approach the dual-carbon signature of the $C_{28:0}$ samples.

$C_{28:0}$ samples of both cores plot very closely together, with no difference in $\delta^{13}C$ and only 60 ‰ (equaling 1100 years) difference in $\Delta^{14}C_{initial.}$ Due to the highly depleted $\delta^{13}C$ values (around -33 ‰), they are situated outside the endmember range on the $\delta^{13}C$ scale. Moreover, the samples lie between the TS-PF and ICD-PF considering the $\Delta^{14}C_{initial}$ values but are closer to the TS-PF endmember. Considering bulk OC samples, they settle between the $C_{16:0}$ and $C_{28:0}$ samples on the $\Delta^{14}C_{initial}$ scale and between the surface and the deeper samples on the $\delta^{13}C$ scale, which is the area covered by the TS-PF endmember. Their radiocarbon content is also much closer to the TS-PF endmember, than to the ICP-PF one.

At last, the proportion of marine organic matter in the samples can be visualized by plotting the isotopic ratios against another (Figure 11). Due to a lack of available data, the endmembers show areas, rather than distinct values. Here, the TS-PF "area" is based on the δ^2H endmember and the Marine OM area based on the $\delta^{13}C$ endmember used by Vonk et al., (2017).
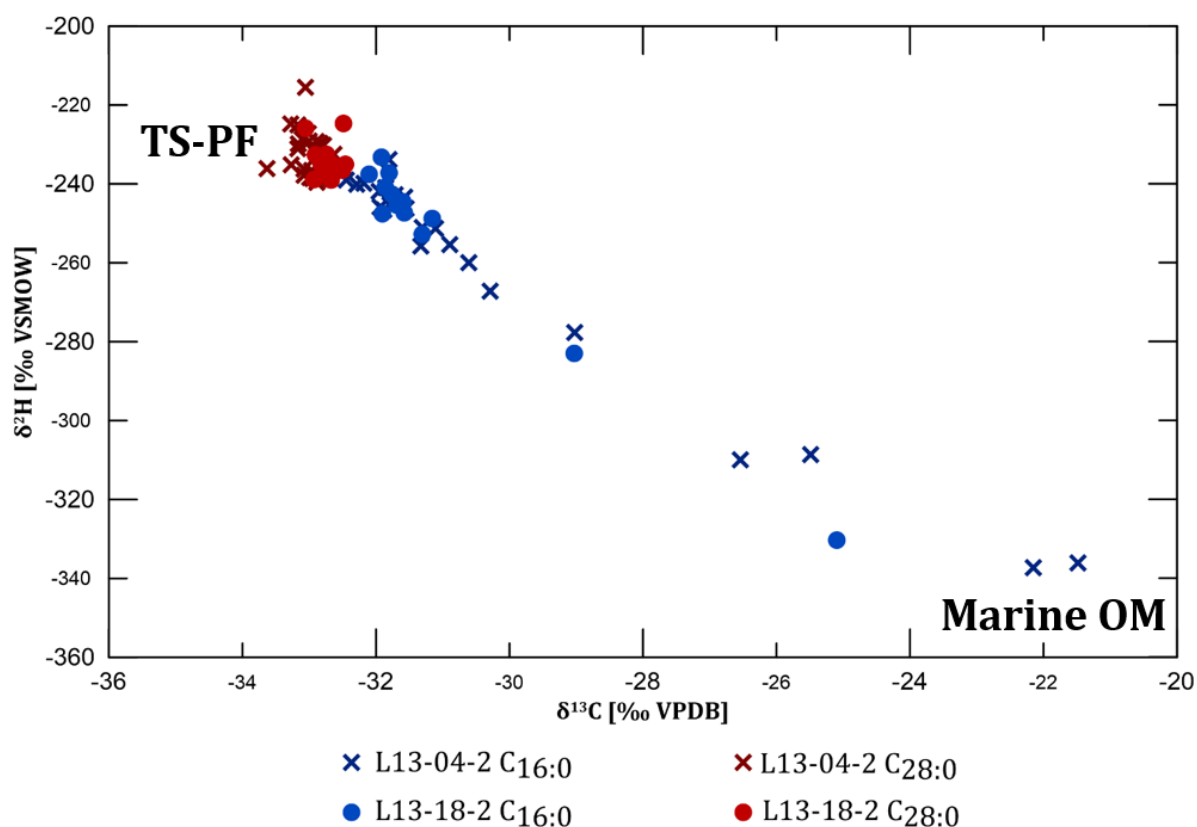
Figure 11: Connection between the two different isotopic ratios δ13C and δ2H as a function of contribution of marine OM. The two endmembers show the estimated areas of the contributing sources.

Like in Figure 9, the distribution of the $C_{16:0}$ samples on the $\delta^{13}C$ scale represents a downcore profile. The surface samples are enriched in ^{13}C and extremely depleted in ^{2}H. With increasing core depths values shift from the range of marine organic matter towards more enriched ^{2}H and more depleted $\delta^{13}C$ values and closer to the $C_{28:0}$ samples. When both isotope ratios are plotted together, there is virtually no distinction possible between the $C_{28:0}$ samples of the two cores. All samples plot in a cluster characterized by deuterium enriched $\delta^{2}H$ and ^{13}C depleted $\delta^{13}C$ values. This cluster covers $\delta^{2}H$ values between -240 and -220 ‰. Remarkably, two samples of core L13-18-2 show slightly enriched $\delta^{2}H$ values compared to the other samples in the core.

4 Discussion

The results suggest an input of $C_{16:0}$ from at least two sources, as demonstrated by the distribution of the samples in the dual carbon plot (Figure 10). There is a markedly dominance from $C_{16:0}$ produced by marine photoautotrophs in the surface samples of both cores, indicated by the strongly enriched $\delta^{13}C$ and $\Delta^{14}C_{initial}$ values. The shift towards more depleted values suggest the input of $C_{16:0}$ from an older source, which is more obvious in Figure 11. It seems that a proportion of $C_{16:0}$ and $C_{28:0}$ could be derived from the same source.

Moving to $C_{28:0}$, the results support the assumption, that the terrigenous biomarker is partially derived from TS-PF and ICD-PF, as shown in Figure 10 by their location in-between the two endmembers. Individual lipids are generally more depleted in ^{13}C compared to bulk OC, due to the specific biosynthesis of *n*-alkanoic acids (J. M. Hayes, 2001). This explains the offset compared to the surface bulk OC measurements. All $C_{28:0}$ samples exhibit the characteristically depleted $\delta^{13}C$ values of C3 plants (Trumbore & Druffel, 1995).

Several hypotheses can be proposed to discuss the results and interpret observed differences between the two cores. In the following, some of these hypotheses are explained and discussed.

Hypothesis 1: Progressing coastal erosion in areas dominated by Pleistocene permafrost deposits suggests an increased proportion of ICD-PF derived organic matter in the sediments.

The accelerated collapse of ICD-PF in close proximity to the core locations is very likely reflected by an increased contribution of old organic material to the sediment in the Laptev Sea, especially in terrestrial derived organic matter, such as the $C_{28:0}$. However, the $\Delta^{14}C_{initial}$ downcore profiles in both cores strongly contradict this theory, as the relatively constant ages of $C_{28:0}$ depict stable

source contribution ratios. The generally higher age of $C_{28:0}$ in core L13-04-2 is a result of the sample site location within the Buor-Khaya Bay, enclosed by intensely eroding Yedoma permafrost deposits, which is reflected in greater accumulation of ICD-PF derived OM compared to core L13-18-2. The HMW ratios in both cores are higher than the value (0.56) van Dongen et al. (2008) calculated for a surface sample collected close to the site of L13-04-2, but are similar to values presented by Karlsson et al. (2011). In ICD-PF, HMW ratios range from 10 to 140 (Vonk et al., 2017), as a result of the conservation from degradation. The lower values calculated for the two cores indicate a moderate degradation of mainly TS-PF derived organic matter throughout the cores. A binary mixing model can be applied to calculate the relative proportions of the two permafrost pools (Figure 12 and Figure 13).

$$\Delta^{14}C_{initial} = x * \Delta^{14}C_{initial}(TS - PF) + (1 - x) * \Delta^{14}C_{initial}(ICD_{PF}) \tag{7}$$

As shown in Figure 9, there is an offset in the position of the $C_{28:0}$ samples on the y-axis, relative to the two endmembers, which is caused by the definition of the endmembers based on bulk measurements. To validate the results obtained using the dual-carbon endmember approach, the same binary model can be applied using the compound specific δ^2H endmembers proposed by Vonk et al., (2017). Those results are depicted in Figure 12 and Figure 13. Both models suggest predominately TS-PF derived input of $C_{28:0}$. There is distinctly less variation in the ratio of contributing sources when the dual-carbon endmembers are used, but this could be due to the limited number of data points and the CRSA measurement of combined samples, which has a mitigating effect on individual variations.
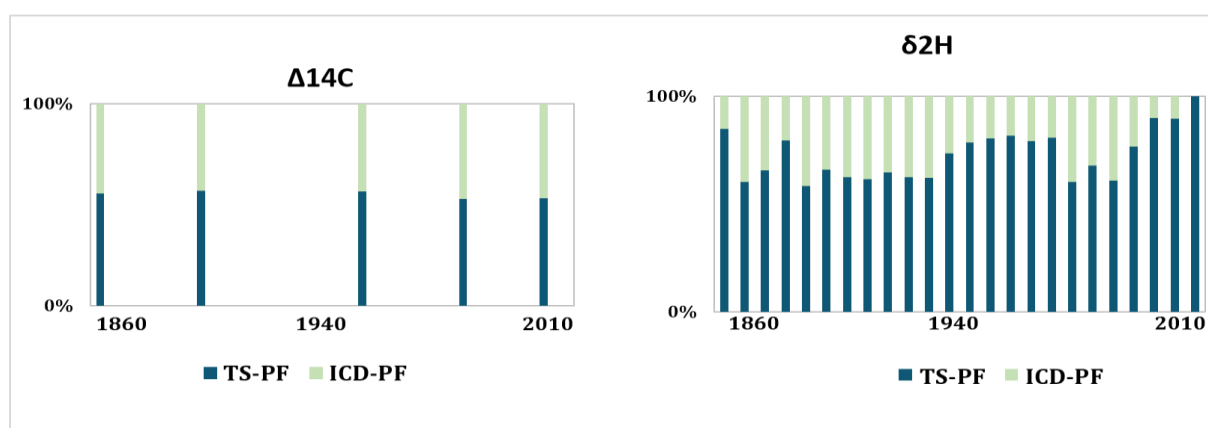
Figure 12: Calculations of the proportions of organic matter derived from TS-PF and ICD-PF for core L13-04-2 using the dual-carbon-endmember approach and the δ2H endmember approach.

Using the dual-carbon approach in L13-04-2 yields a TS-PF derived proportion of 55%, while results of the δ^2H model suggest 73% of TS-PF derived input.
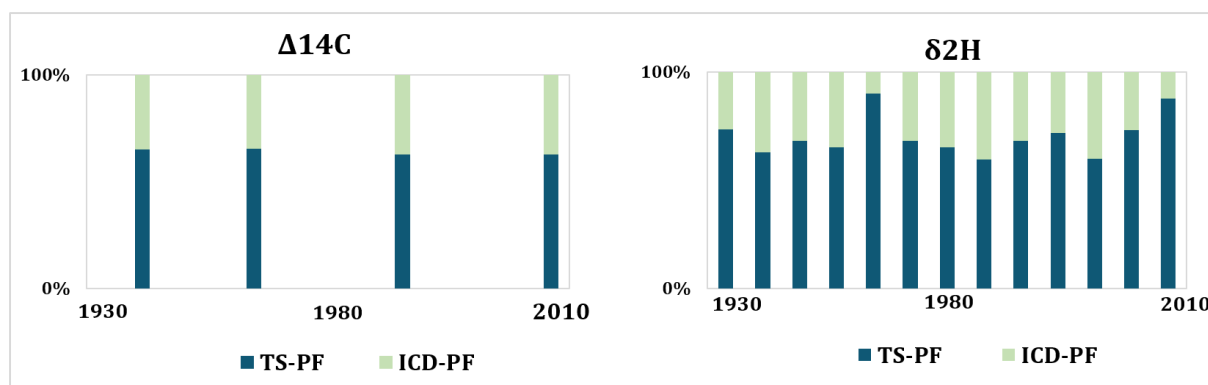
Figure 13: Calculations of the proportions of organic matter derived from TS-PF and ICD-PF for core L13-18-2 using the dual-carbon-endmember approach and the δ2H endmember approach.

In core L13-18-2, results of the two models agree better, suggesting 64% (dual-carbon-approach) and 70% (δ^2H approach) of TS-PF input respectively. Although there is more variation in the δ^2H models, the results suggest no increased deposition of ICD-PF over the last century. There is a marked increase in TS-PF contribution in the upper parts of both cores. A possible reason explaining this trend is discussed later.

The results obtained in this study contradict an increased input of ICD-PF derived organic matter. Yet, the extensive collapse of ICD-PF is well documented and it is inevitable that the contained organic matter is translocated into the Laptev Sea (i.e. through island collapse). If the radiocarbon content of $C_{28:0}$ is not reflecting this progressive erosion of old permafrost, the explanation is either an alteration (i.e. degradation) of the organic matter or sequestration at a different location. During their investigation of the erosion of Moustakh Island Vonk et al., (2012) discovered extensive degradation of organic matter released from the permafrost at site. They suggest that as much as 66% of OC is lost during the downslope degradation occurring on the cliff slopes of the island. This finding is in contrast to the assumption that allochthonous terrestrial material is rather protected from degradation due to its association with mineral phases (Hedges et al., 1999). Furthermore, it is assumed that mineral associated organic matter derived from coastal erosion settles rapidly and in proximity to the shore (Vonk et al., 2010).

ICD-PF derived matter can also be discharged into the Laptev Sea by the river itself, as part of the catchment area is composed of Yedoma, which is also likely to be affected by climate change. However, it is under debate how much of the suspended material actually reaches the Arctic Ocean. Alabyan et al. (1995) found that as little 10-17% of the original suspended matter load is actually discharged directly, while the remainder is temporarily deposited in the delta. Though this figure might be subject to change over time and under the influence of increasing water discharge, it is likely that suspended matter is deposited in the delta for at least some time, which could be a possible retaining mechanism for heavier, mineral associated organic matter. Another

possible explanation for the constant source ratios could be the overall increased input from both sources. However, the constant mass accumulation rates of $C_{28:0}$ contradict this theory.

Hypothesis 2: There is an increased input of terrestrial organic matter derived from a more southern location in the catchment area.

The stable hydrogen isotopic composition of organic matter is determined by the composition of the water source used by the organism. Environmental water, such as precipitation water or ocean water is the main hydrogen source for photoautotrophs. The isotopic composition of precipitation exhibits strong spatial variability due to fractionation between evaporation and condensation of water (Gat, 1996). During evaporation of seawater ($\delta^2H=0$‰), water containing the lighter isotope ^1H evaporates faster, resulting in a depleted isotopic composition of the vapor. When the vapor condenses as precipitation, water containing the heavier isotope ^2H condenses faster, resulting in an isotopic enriched composition of the precipitation. Dansgaard (1964) described a continental effect on the regional composition of precipitation. Water vapor containing air masses travelling overland successively loses water as precipitation, resulting in a progressing depletion of the vapor over time. The resulting precipitation is also progressively depleted. Figure 14 shows the contemporary annual δ^2H composition of precipitation in Asia and an enlarged part is showingthe Lena Delta region.
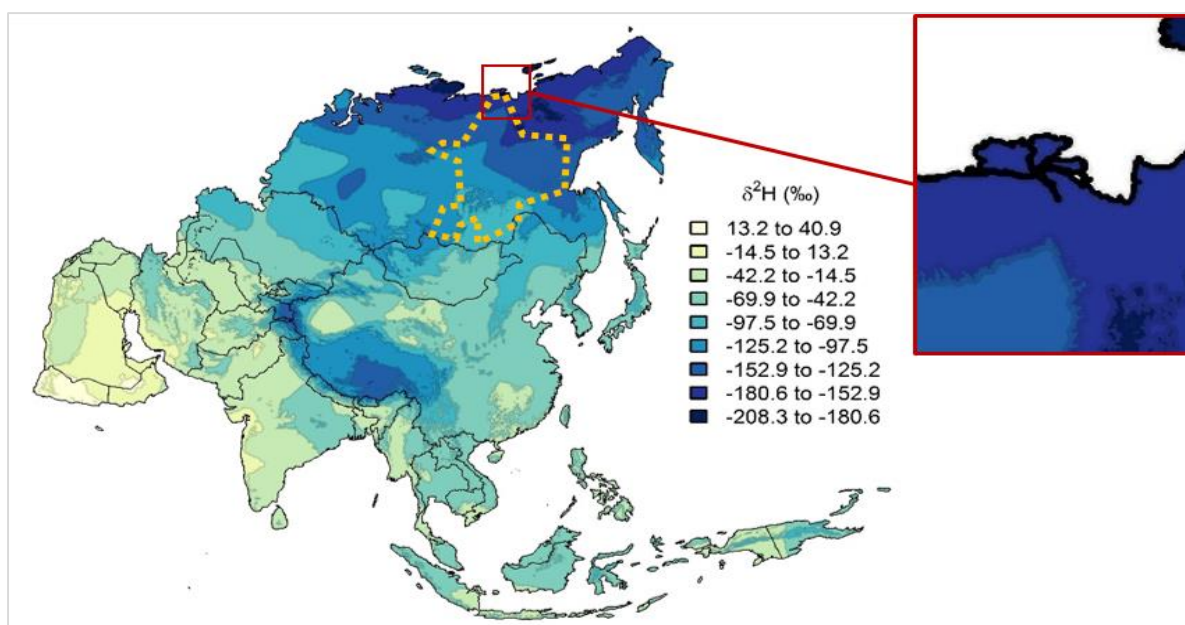
Figure 14: δ2H of the annual precipitation in Asia (Waterisotopes Database (2018); http://www.waterisotopes.org, retrieved 20 May 2018). The catchment area is indicated by the dashed orange line and the detail picture shows the Lena delta.

It is important to note that the displayed δ^2H variations might not be representative for the climatic conditions at the time the $C_{28:0}$ was produced. However, a general trend of progressing isotopic depletion in precipitation can be assumed. As the Figure 14 shows, the δ^2H signature of precipitation varies greatly in the Lena catchment area, with progressing δ^2H depletion from south to north. In the area close to the delta, values show already variations of up to 80 ‰ (detailed picture in Figure 14). It can be assumed that organic matter reflects the general location of its production in the catchment area (i.e. rather north or rather south) in its hydrogen isotopic composition.

It is possible to reconstruct the isotopic composition of the water source, if the organism specific fractionation pattern during synthesis of a certain compound is known. Sachse et al. (2004) describe a constant fractionation pattern in long-chain n-alkanes along a European north-south transect, suggesting that the fraction is independent of environmental changes. However, Sessions et al. (1999) describe different fractionation for n-alkanoic acids and n-alkanes in the same organism, resulting in differences in the δ^2H values of both compounds of up to 50‰. Hence, it is more complicated to calculate the isotopic composition of the water source based on n-alkanoic δ^2H values. Since this calculation would be highly speculative and probably include many assumptions, instead the relative deviation of $C_{28:0}$ δ^2H values in the two cores can be used. In both cores, there is an increase of δ^2H in the surface sediment, but due to higher overall fluctuation in core L13-18-2, this increase might not exhibit an actual trend.

In L13-04-2, the increase is more pronounced, resulting in a difference of 20‰ between the surface sample and the average of the core. This could indicate the input of $C_{28:0}$ produced in an area were precipitation is up to 20‰ more enriched in ^2H compared to the area, where most of the $C_{28:0}$ in core L13-04-2 is produced.

The constant $\Delta^{14}C_{initial}$ values of $C_{28:0}$ suggest that the proportion of TS-PF that contributes organic matter has not increased. However, it seems that there is increasingly more input of TS-PF from more southern parts of the catchment. Although this interpretation is highly speculative, it explains the differences between the source ratio models described earlier. It shows that the results obtained with the δ^2H endmember approach generally verify the dual-carbon results but are also susceptible to changes within one of the endmember pools, without necessarily reflecting a change in the proportion of contribution.

Hypothesis 3: Changes in the concentration and stable isotopic composition of $C_{16:0}$ are mainly caused by preferential degradation.

A number of processes could be responsible for the pronounced rise in the $C_{16:0}$ concentrations in the top part of both cores. It is possible that increased contribution of a source pool containing great amounts of $C_{16:0}$, such as ICD-PF, caused this change. Vonk et al. (2017) measured $C_{16:0}$

concentrations of 1750 µg/gTOC in an ICD-PF sample located within the Lena Delta and increased erosion of these deposits would most likely be reflected in the core concentrations. However, this scenario seems unlikely since there is no evidence in the $\Delta^{14}C_{initial}$ signal, suggesting input of older material. Another reason for the high concentrations could be an increase in primary production, induced by a permafrost thaw related release of nutrients, an effect reported in numerous studies (i.e Hobbie et al., 1999; Keller et al., 2007; Reyes & Lougheed, 2015).

If these excess nutrients were discharged into the Laptev Sea, they would likely propel primary production. Due to the huge amount of suspended matter discharged by the Lena, water transparency decreases drastically in the Buor-Khaya Bay, thereby reducing primary production to the first meters below the surface (Sorokin & Sorokin, 1996). The low temperatures and short vegetative season further restrain primary production. In addition, Vonk et al., (2014) describe ongoing degradation of fresh marine and riverine particulate organic matter during settling, reducing the proportion of fresh biogenic matter that is deposited in sediments. Considering these findings, it seems unlikely that enhanced primary production is the sole cause of the increased $C_{16:0}$ concentrations.

The most plausible process underlying the concentration trend is preferential degradation of recently produced marine OM. Compared to the recalcitrant allochthonous terrestrial organic compounds, recently produced organic compounds are more reactive and are subject to preferential microbial degradation. The different concentration profiles observed in the two cores suggest a higher degradation rate in L13-18-2 than in L13-04-2.

Bottom water oxygen concentration (BWOC) and the resulting oxygen exposure time of OM have a major driving influence on degradation rates (Hartnett et al., 1998). Respiration of organic matter at the sediment-water boundary is an oxygen consuming process that results in lower degradation rates in the underlying sediment. During transect measurements in the Laptev Sea, Semiletov et al. (2013) measured extremely low oxygen saturations in the bottom water of the Buor-Khaya Bay and higher concentrations further north in the Laptev Sea (Figure 15). Inferred from this, BWOC is about twice as high at the site of L13-18-2 compared to L13-04-2. This suggests, that degradation at the sediment-water interface is higher at the site of L13-04-2, which is corroborated by the lower concentration of $C_{16:0}$ in the surface sample. The differences in BWOC explain the unequal degradation rates in the two cores.
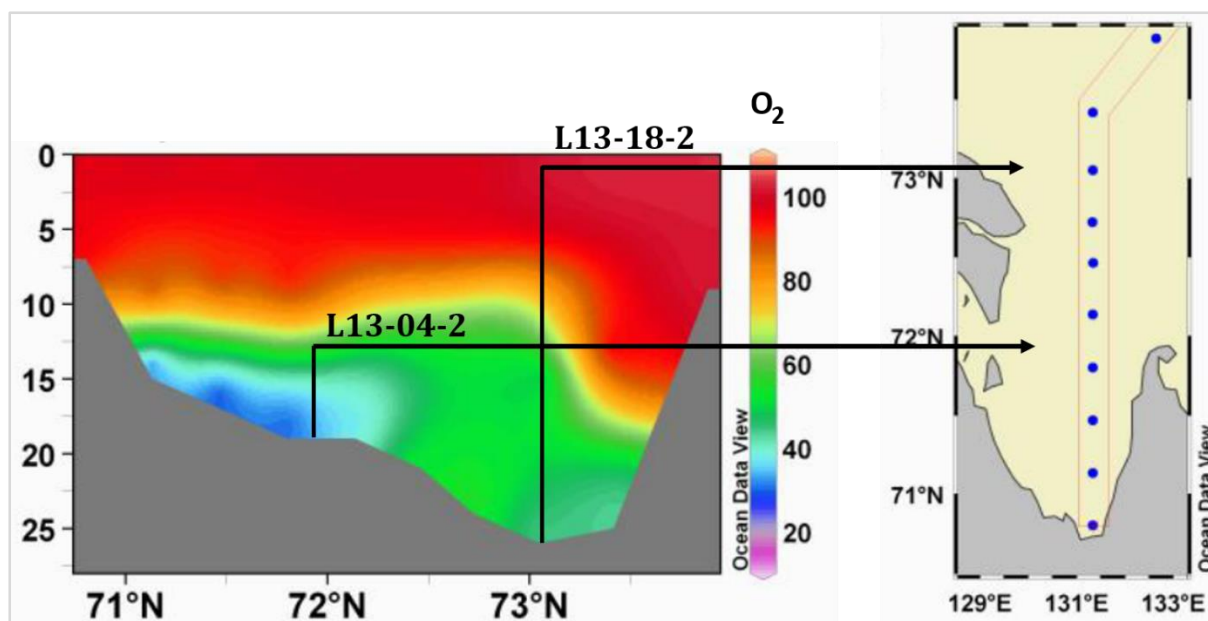
Figure 15: Ocean water oxygen saturation [%] measured along a south-north transect through the Buor-Khaya Bay and the Laptev Sea. The labelled arrows show the location of cores studied here and the inferred BWOC. Figures are taken from Semiletov et al. (2013).

Hypothesis 4: Due to a lower degradation rate in L13-04-2, the $C_{16:0}$ profile is strongly influenced by the excess ^{14}C produced during nuclear weapon tests.

In order to discuss the $\Delta^{14}C_{initial}$ profiles of the $C_{16:0}$ samples, it is important to determine the core depth in which degradation terminates. Due to the exponential decrease of the degradation rates, it is difficult to use the concentration profiles alone, since variation in the lower parts of the cores are so insignificant, that differentiation between a trend and the uncertainty of the quantification is purely based on estimation. A noticeable feature of the stable isotopic compositions in both cores are the quasi-identical values measured in $C_{16:0}$ and $C_{28:0}$. The converging values of the two *n*-alkanoic acids displayed in Figure 10 as a result of the decreasing proportion of recently produced organic matter suggest a common source for $C_{16:0}$ and $C_{28:0}$ that exhibits terrestrial characteristics.

Hence, the degradation is reflected by a change of the isotopic composition of $C_{16:0}$ from characteristically marine (enriched $\delta^{13}C$ and depleted $\delta^{2}H$ values) to characteristically terrigenous (depleted $\delta^{13}C$ and enriched $\delta^{2}H$). It is likely that degradation has ceased when there is no difference in the stable isotopic composition of $C_{16:0}$ and $C_{28:0}$, which appears to be around the year 1980 in core L13-18-2, based on the $\delta^{13}C$ values and around the year 1940 in L13-04-2.

This assumption is supported by the β-sitosterol indices of the cores. Lower values are caused by increased concentration of the marine biomarkers brassicasterol and dinosterol. In both cores, the values increase with core depth as the marine sterols are degraded. The trend is less steep in L13-04-2 but is perceptible from the core top to sediments deposited between 1940 and 1950.

33

The general offset is due to the higher rate of primary production as a result of the location of L13-04-2 close to the channel discharging most of the suspended matter and nutrients. This results in higher primary production and therefore lower β-sitosterol index values. In core L13-18-2 the transition from increasing to constant values can be determined depending on the differences between the single values. Differences between sediment samples deposited between 1980 and 2012 range from 0.2-0.5. After 1980 differences decrease to 0-0.1.

These findings suggest that contemporarily produced marine organic matter is in very small amounts present in sediments deposited as early as 1940-1950 (L13-04-2) and 1980 (L13-18-2), which is also reflected in the $\Delta^{14}C_{initial}$ profiles of $C_{16:0}$ in the two cores. In general, a bigger proportion of recently produced OM results in increased $\Delta^{14}C_{initial}$ values. In L13-04-2, the major rise in $\Delta^{14}C_{initial}$ occurs between sediment deposited in 1900 and 1940, whereas in L13-18-2 distinctly higher values were measured in samples deposited after 1980. Although the slower degradation of young $C_{16:0}$ in L13-04-2 explains the earlier onset of a rise in $\Delta^{14}C_{initial}$ in that core, it does not account for the magnitudes of increment compared to L13-18-2.

Extensive testing of nuclear weapons in the 1950s and 1960s doubled the concentration of radiocarbon in the atmosphere within a decade (Goodsite et al., 2001). This rapid increase is referred to as the Bomb Pulse. Since the tests terminated, the surplus of radiocarbon is decaying and the atmospheric radiocarbon concentration is thought to reach pre-test levels around the year 2030 (Graven, 2015). The artificially generated excess ^{14}C is reflected in organic matter that was produced since the tests were carried out. The signal can be detected until the compound is degraded.

It is therefore depending on the degradation rate, if the Bomb Pulse can be distinctly identified in the $\Delta^{14}C_{initial}$ profile of a compound. Figure (16) shows the possible influence of the Bomb Pulse on a sediment core that contains $C_{16:0}$ that is partially derived from a recent source (marine production) and from an old source (permafrost), to investigate possible similarities with the profiles of the two cores.
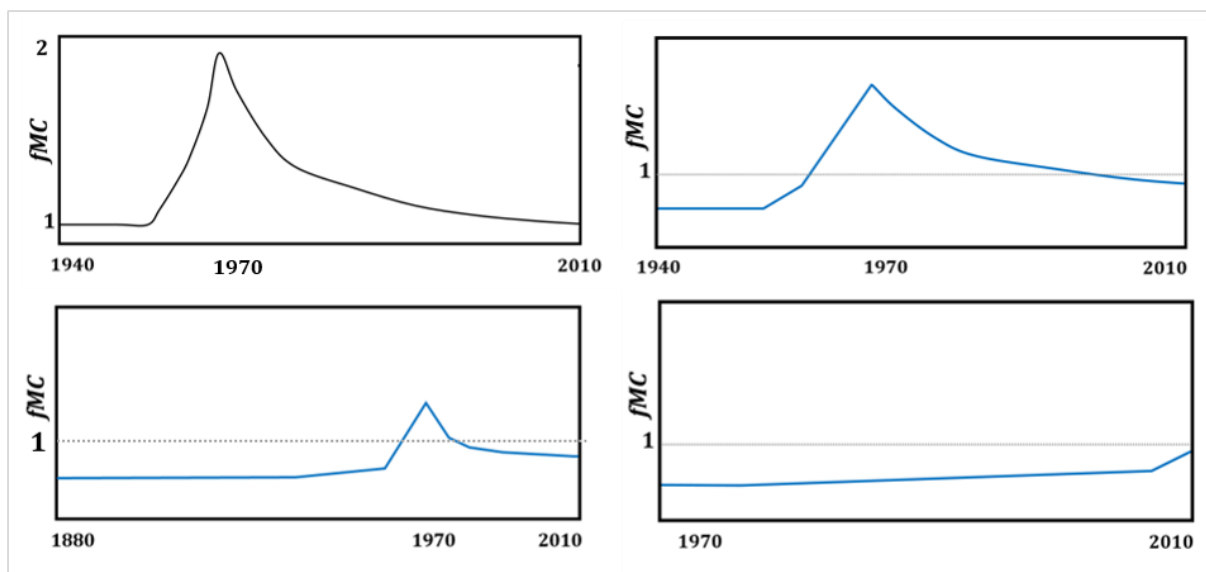
Figure 16: Possible influences of the Bomb Pulse on the $\Delta^{14}C_{initial}$ of $C_{16:0}$ that is derived partly from recent production and partly from a permafrost source in different scenarios.
A: Development of the atmospheric 14C concentration as a result of nuclear weapon testing (Bomb Pulse), changed after Goodsite et al. (2001).
B-C: Bomb Pulse influence in a sediment with no degradation (B), low-rate degradation (C) and high-rate degradation (D).

When there is no degradation, the $\Delta^{14}C_{initial}$ profile should resemble the atmospheric radiocarbon concentration. Around 1940, the $\Delta^{14}C_{initial}$ displays the proportions of the old and the young source. Around 1970, the Bomb Pulse is reflected as a sharp peak and after 1970, the influence of the excess ^{14}C subsides. Eventually, around the year 2030 (not displayed) $C_{16:0}$ should have the same value as $C_{16:0}$ deposited around 1940. Degradation should have a mitigating effect on the shape of the profile (Picture C). If degradation is still progressing in sediment deposited around 1940, this should be reflected in a slight increase of $\Delta^{14}C_{initial}$ in the sediment deposited after 1940, followed by some sort of distinct peak around the time of the tests.

The trend after the Bomb Pulse then depends on the degradation rate, but there should be a visible decrease. When the degradation rate is high and all $C_{16:0}$ produced during the time of testing is consumed, a steadier $\Delta^{14}C_{initial}$ profile is likely (Figure 12, picture D). There would be no distinct peak and values would decrease downcore from the surface, with the slope depending on the degradation rate. However, since degradation is usually highest in the first cm of a sediment core, it is likely that the loss of a great proportion of recently produced matter is reflected in a distinct decrease of $\Delta^{14}C_{initial}$ values.

Based on the expected influence of different degradation rates on the $\Delta^{14}C_{initial}$ trends, L13-04-2 should exhibit a profile resembling picture C and L13-18-2 should exhibit a profile similar to the one in picture D. While $C_{16:0}$ in L13-18-2 shows the expected resemblance, there is no pronounced peak in the $C_{16:0}$ profile of L13-04-2. As a result of CRSA measurement of samples comprising multiple depths, the number of sample point is very limited and the values include the radiocarbon signal of up to 10 years (Table 2). In L13-04-2, this leads to lack in data coverage

during the time of the Bomb-Pulse. It is likely that in L13-04-2 samples deposited between 1960 and 1970 would exhibit anomalously high radiocarbon contents.

The assumption, that degradation of young $C_{16:0}$ has ceased around 1980 in L13-18-2, is supported by the steady $\Delta^{14}C_{initial}$ trend. Since there is no more $C_{16:0}$ produced during the time of the tests, there is no excess ^{14}C that could lead to extremely enriched $\Delta^{14}C_{initial}$ values. While the influence of the Bomb-Pulse thus explains the overall higher radiocarbon content in L13-04-2 after 1970, the sample deposited around 1940 shows a surprisingly high radiocarbon content. This cannot be explained by Bomb-Pulse influence, since the test started after 1953. A possible reason for the unexpectedly high $\Delta^{14}C_{initial}$ value could be bioturbation, resulting in the translocation of young organic matter in deeper parts of the core.

A surprising observation in both cores is the high radiocarbon content in depths, were there is almost no recently produced $C_{16:0}$ left. It is striking that the high rate of degradation in the first cm of both cores is not reflected in a sharp decrease of $\Delta^{14}C_{initial}$. It should be expected that the extreme loss of $C_{16:0}$ below the surface of the core is reflected in a severe loss of radiocarbon.

5 Conclusion

Overall, the results of this study suggest distinct differences in the geochemical characteristics of the two cores. Both sites receive their main organic matter input from TS-PF, although in different proportions.

Decreasing $\Delta^{14}C$ values of $C_{28:0}$ could not be found in either of the cores. Both permafrost pools contribute organic matter and therefore influence the $\Delta^{14}C$ values of $C_{28:0}$. Core L13-04-2 was recovered from a location close to active erosion sites of ICD-PF, which is reflected in generally more depleted $\Delta^{14}C$ values compared to L13-18-2. Increased accumulation of ICD-PF derived organic matter would likely be reflected in lower $\Delta^{14}C$ values, however this expected trend could not be confirmed. Two binary mixing models using different endmembers were applied to calculate the source proportions. These calculations yield comparable results and suggest that TS-PF contributes the major proportion of organic matter. Nevertheless, the extensive collapse of ICD-PF is progressing. Reasons for this obvious discrepancy could be down slope degradation of ICD-Pf or sequestration in closer proximity to the erosion sites.

The measurements of δ^2H of $C_{28:0}$ in core L13-04-2 show a distinct trend towards more enriched values, which suggest a change in the contributing source during the last decade. A possible explanation is an increased contribution of organic matter derived from a more southern location in the catchment. Precipitation is increasingly more depleted in ^2H towards the delta, which leads to the production of ^2H enriched matter further south. Finding enriched organic matter in the core

could thus suggest a more southern origin. Although more enriched values were also recognizable in the surface of L13-18-2, it is more complicated to characterize this finding as a distinct trend. It is important to notice that there are other explanations possible.

Changes in the stable isotopic composition and the concentration of $C_{16:0}$ can be caused by three different processes. The first is increased contribution of a source containing high concentrations of $C_{16:0}$, such as ICD-PF. However, this is contradicted by highly enriched radiocarbon contents in the respective samples. Another reason could be increased primary production, which is unlikely due to high rate degradation of recently produced organic matter during settling and limitations to primary production in the Arctic. Hence, preferential degradation is the most plausible reason for the changing profiles. The results suggest a higher degradation rate in L13-18-2, which is supported by previously conducted studies.

Caused by the high degradation rate in L13-18-2, recently produced $C_{16:0}$ is not present in sediment deposited before 1980. In contrast, lower the degradation rate in L13-04-2 results in a longer preservation of young $C_{16:0}$, which seems to be present in samples deposited as early as 1940. Therefore, the excess 14C produced by nuclear weapon tests is strongly reflected in the radiocarbon content of $C_{16:0}$ in L13-04-2. The steady profile in L13-18-2 supports this assumption.

Problems occurring in the interpretation of the radiocarbon results is the lack of data points and the measurement of mixed samples. Comparing the radiocarbon data points that comprise sample information of up to 10 years with individual data points from the stable isotope measurements is complicated and is likely to result in interpretation discrepancies. Therefore a more substantial and profound interpretation would be possible, if the radiocarbon dating could be conducted on every single sediment sample.

6 Acknowledgements

I want to thank Gesine Mollenhauer for supervising my Bachelor Thesis and for the support and guidance I have received during the last two years. It is a great pleasure to be part of your working group and I cannot imagine a better working place.

Furthermore, I would like to thank Enno Schefuß for your supervision and the time you have invested to discuss my findings. I am very grateful I had the chance to get to know a completely new field of research at your facilities.

I would like to thank Hendrik Grotheer for the time you have invested in helping me with this thesis. During the last years, you were not only a great and patient teacher but also an amazing friend. Thank you for your unconditional support.

Additionally, I want to thank Jens Hefter, Torben Gentz, Vera Meyer and Ralph Kreutz for your help with the lab work and for your extensive explanations.

I want to thank Lukas, for proof reading and giving helpful comments. I am very grateful for your tremendous support across the distance and the amount of time and thoughts you put into this. And of course, thank you for a remarkable friendship!

Moreover, I want to thank Sarah for your encouragement and sympathy during the last month and for your friendship during the last years.

At last, I want to thank Silvio for proof reading and helping me, when I was lost for words. Thank you so much for the time you invested and for your advises from an outside perspective. But above all I want to thank you for always standing by my side.

7 References

Alabyan, A. M., Chalov, R. S., Korotaev, V. N., Sidorchuk, A. Y., & Zaitsev, A. A. (1995). Natural and technogenic water and sediment supply to the Laptev Sea. *Bericht Polarforschung*, (176), 265–271.

Anisimov, O., & Reneva, S. (2006). Permafrost and Changing Climate: the Russian Perspective. *AMBIO A Journal of the Human Environment*, *35*(7), 381–7. http://doi.org/10.1579/0044-7447(2006)35[169:PACCTR]2.0.CO;2

Bröder, L., Tesi, T., Andersson, A., Semiletov, I., & Gustafsson, Ö. (2018). Bounding cross-shelf transport time and degradation in Siberian-Arctic land-ocean carbon transfer. *Nature Communications*, *9*(1). http://doi.org/10.1038/s41467-018-03192-1

Burn, C. R. (1998). The active layer: Two contrasting definitions. *Permafrost and Periglacial Processes*, *9*(4), 411–416. http://doi.org/10.1002/(SICI)1099-1530(199810/12)9:4<411::AID-PPP292>3.0.CO;2-6

Costard, F., & Gautier, E. (2007). The Lena river: Hydromorphodynamic Features in a Deep Permafrost Zone. In A. Grupta (Ed.), *Large Rivers – Geomorphology and Maganagement* (pp. 225–232). West Sussex, England: John Wiley & Sons. http://doi.org/10.1002/9780470723722.ch5

Cranwell, P. A., Eglinton, G., & Robinson, N. (1987). Lipids of aquatic organisms as potential contributors to lacustrine sediments-II. *Organic Geochemistry*, *11*(6), 513–527. http://doi.org/10.1016/0146-6380(87)90007-6

Dansgaard, W. (1964). Stable isotopes in precipitation. *Tellus*, *16*(4), 436–468. http://doi.org/10.3402/tellusa.v16i4.8993

Eglinton, G., & Hamilton, R. J. (1967). Leaf Epicuticular Waxes. *Science*, *156*(3780), 1322–1335. http://doi.org/10.1126/science.156.3780.1322

Gat, J. R. (1996). Oxygen and Hydrogen Isotopes in the Hydrologic Cycle. *Annu. Rev. Earth Planet. Sci.*, *24*, 225–262. http://doi.org/10.1146/annurev.earth.24.1.225

Goodsite, M. E., Rom, W., Heinemeier, J., Lange, T., Ooi, S., Appleby, P. G., … Hansen, T. S. (2001). High-Resolution AMS 14C Dating of Post-Bomb Peat Archives of Atmospheric Pollutants. *Radiocarbon*, *43*(2B), 495–515. http://doi.org/10.1017/S0033822200041163

Graven, H. D. (2015). Impact of fossil fuel emissions on atmospheric radiocarbon and various applications of radiocarbon over this century. *Proceedings of the National Academy of Sciences*, *112*(31), 9542–9545. http://doi.org/10.1073/pnas.1504467112

Günther, F., Overduin, P. P., Baranskaya, A., Opel, T., & Grigoriev, M. N. (2013). Observing Muostakh Island disappear: erosion of a ground-ice-rich coast in response to summer warming and sea ice reduction on the East Siberian shelf. *The Cryosphere Discussions*, *7*(4), 4101–4176. http://doi.org/10.5194/tcd-7-4101-2013

Han, P. (2014). Characteristics and sedimentation rates at the shallow Laptev Sea.

Hartnett, H., Keil, R., Hedges, J., & Devol, A. (1998). Influence of oxygen exposure time on organic carbon preservation in continental margin sediments. *Nature*, *391*(February), 572–575. http://doi.org/10.1038/35351

Hayes, J. M. (1993). Factors controlling 13 C contents of sedimentary organic compounds: Principles and evidence. *Marine Geology*, *113*(1), 111–125. http://doi.org/10.1016/0025-3227(93)90153-M

Hayes, J. M. (2001). Fractionation of Carbon and Hydrogen Isotopes in Biosynthetic Processes.

Reviews in Mineralogy and Geochemistry, *43*(1), 225–277. http://doi.org/10.2138/gsrmg.43.1.225

Hayes, J. M. (2002). Practice and principles of isotopic measurements in organic geochemistry. *Organic Geochemistry of Contemporaneous and Ancient Sediments*, *5*(August), e5. http://doi.org/10.2307/1938584

Hedges, J. I., Hu, F. S., Devol, A. H., Hartnett, H. E., Tsamakis, E., & Keil, R. G. (1999). Sedimentary organic matter preservation: A test for selective degradation under oxic conditions. *American Journal of Science*, *299*(7–9), 529–555. http://doi.org/10.2475/ajs.299.7-9.529

Hobbie, J. E., Peterson, B. J., Bettez, N., Deegan, L., O'Brien, W. J., Kling, G. W., … Hershey, A. E. (1999). Impact of global change on the biogeochemistry and ecology of an Arctic freshwater system. *Polar Research*, *18*(2), 207–214. http://doi.org/10.3402/polar.v18i2.6576

Hugelius, G., Strauss, J., Zubrzycki, S., Harden, J. W., Schuur, E. A. G., Ping, C. L., … Kuhry, P. (2014). Estimated stocks of circumpolar permafrost carbon with quantified uncertainty ranges and identified data gaps. *Biogeosciences*, *11*(23), 6573–6593. http://doi.org/10.5194/bg-11-6573-2014

Hwang, J., & Druffel, E. R. M. (2005). Blank Correction for Δ14 C measurements in organic compound classes of oceanic particulate matter. *Radiocarbon*, *47*(1), 75–87. http://doi.org/10.1017/S0033822200052218

Jorgenson, M. T., H. Racine, C., C. Walters, J., & Osterkamp, T. (2001). Permafrost Degradation and Ecological Changes Associated With a Warming Climate in Central Alaska. *Climatic Change*, *48*, 551–579.

Karlsson, E. S., Charkin, A., Dudarev, O., Semiletov, I., Vonk, J. E., Sánchez-García, L., & Andersson, A. (2011). Carbon isotopes and lipid biomarker investigation of sources, transport and degradation of terrestrial organic matter in the Buor-Khaya Bay, SE Laptev Sea. *Biogeosciences*, *8*(7), 1865–1879. http://doi.org/10.5194/bg-8-1865-2011

Keller, K., Blum, J. D., & Kling, G. W. (2007). Geochemistry of Soils and Streams on Surfaces of Varying Ages in Arctic Alaska. *Arctic, Antarctic, and Alpine Research*, *39*(1), 84–98. http://doi.org/10.1657/1523-0430(2007)39[84:GOSASO]2.0.CO;2

McGuire, A. D., Anderson, L. G., Christensen, T. R., Dallimore, S., Guo, L., Hayes, D. J., … Roulet, N. (2009). Sensitivity of the Carbon Cycle in the Arctic to Climate Change. *Ecological Monographs*, *79*, 523–555.

Pittauer, D. (2018). *Cores 04 and 18 2018_03*.

Reyes, F. R., & Lougheed, V. L. (2015). Rapid Nutrient Release from Permafrost Thaw in Arctic Aquatic Ecosystems. *Arctic, Antarctic, and Alpine Research*, *47*(1), 35–48. http://doi.org/10.1657/AAAR0013-099

Rieley, G., Collier, R. J., Jones, D. M., Eglinton, G., Eakin, P. A., & Fallick, A. E. (1991). Sources of sedimentary lipids deduced from stable carbon-isotope analyses of individual compounds. *Nature*. http://doi.org/10.1038/352425a0

Sachse, D., Radke, J., & Gleixner, G. (2004). Hydrogen isotope ratios of recent lacustrine sedimentary n-alkanes record modern climate variability. *Geochimica et Cosmochimica Acta*, *68*(23), 4877–4889. http://doi.org/10.1016/j.gca.2004.06.004

Schirrmeister, L., Grosse, G., Wetterich, S., Overduin, P. P., Strauss, J., Schuur, E. A. G., & Hubberten, H. W. (2011). Fossil organic matter characteristics in permafrost deposits of the northeast Siberian Arctic. *Journal of Geophysical Research: Biogeosciences*, *116*(3). http://doi.org/10.1029/2011JG001647

Schuur, E., Bockheim, J., & Canadell, J. (2008). Vulnerability of permafrost carbon to climate change: Implications for the global carbon cycle. ..., *58*(8), 701. http://doi.org/10.1641/B580807

Semiletov, I. P., Shakhova, N. E., Pipko, I. I., Pugach, S. P., Charkin, A. N., Dudarev, O. V., … Nishino, S. (2013). Space-time dynamics of carbon and environmental parameters related to carbon dioxide emissions in the Buor-Khaya Bay and adjacent part of the Laptev Sea. *Biogeosciences*, *10*(9), 5977–5996. http://doi.org/10.5194/bg-10-5977-2013

Sessions, A. L., Burgoyne, T. W., Schimmelmann, A., & Hayes, J. M. (1999). Fractionation of hydrogen isotopes in lipid biosynthesis, Org. *Organic Geochemistry*, *30*, 1193–1200. http://doi.org/10.1016/S0146-6380(99)00094-7

Shiklomanov, A. I., Holmes, R. M., McClelland, J. W., Tank, S. E., & Spencer, R. G. M. (2018). ArcticGRO Discharge Dataset.

Sorokin, Y. I., & Sorokin, P. Y. (1996). Plankton and primary production in the Lena River Estuary and in the south-eastern Laptev sea. *Estuarine, Coastal and Shelf Science*, *43*(4), 399–418. http://doi.org/10.1006/ecss.1996.0078

Strauss, J., Schirrmeister, L., Grosse, G., Fortier, D., Hugelius, G., Knoblauch, C., … Veremeeva, A. (2017). Deep Yedoma permafrost: A synthesis of depositional characteristics and carbon vulnerability. *Earth-Science Reviews*, *172*(July), 75–86. http://doi.org/10.1016/j.earscirev.2017.07.007

Stuiver, M., & Polach, H. A. (1977). Discussion: reporting of 14 C data. *Radiocarbon*, *19*(3), 355–363. http://doi.org/10.1021/ac100494m

Synal, H.-A., Stocker, M., & Suter, M. (2007). MICADAS: A new compact radiocarbon AMS system. *Nuclear Instruments and Methods in Physics Research, Section B: Beam Interactions with Materials and Atoms*, *259*(1), 7–13. http://doi.org/10.1016/j.nimb.2007.01.138

Tananaev, N. I., Makarieva, O. M., & Lebedeva, L. S. (2016). Trends in annual and extreme flows in the Lena River basin, Northern Eurasia. *Geophysical Research Letters*, *43*(20), 10,764-10,772. http://doi.org/10.1002/2016GL070796

Tarnocai, C., Canadell, J. G., Schuur, E. A. G., Kuhry, P., Mazhitova, G., & Zimov, S. (2009). Soil organic carbon pools in the northern circumpolar permafrost region. *Global Biogeochemical Cycles*, *23*(2), 1–11. http://doi.org/10.1029/2008GB003327

Trumbore, S. E., & Druffel, E. R. M. (1995). Carbon isotopes for characterizing sources and turnover of nonliving organic matter. In R. G. Zepp, & C. Sonntag (Eds.), Role of Nonliving Organic Matter in the Earth's Carbon Cycle (pp. 7-22). Chichester: John. (1995), 1995.

van Dongen, B. E., Semiletov, I., Weijers, J. W. H., & Gustafsson, Ö. (2008). Contrasting lipid biomarker composition of terrestial organic matter exported from across the Eurasian Arctic by the five great Russian Arctic rivers. *Global Biogeochemical Cycles*, *22*(1), 1–14. http://doi.org/10.1029/2007GB002974

Volkman, J. K. (1986). A review of sterol markers for marine and terrigenous organic matter. *Organic Geochemistry*, *9*(2), 83–99. http://doi.org/10.1016/0146-6380(86)90089-6

Vonk, J. E., Sanchez-Garca, L., Van Dongen, B. E., Alling, V., Kosmach, D., Charkin, A., … Gustafsson, A. (2012). Activation of old carbon by erosion of coastal and subsea permafrost in Arctic Siberia. *Nature*, *489*(7414), 137–140. http://doi.org/10.1038/nature11392

Vonk, J. E., Sánchez-García, L., Semiletov, I., Dudarev, O., Eglinton, T., Andersson, A., & Gustafsson, O. (2010). Molecular and radiocarbon constraints on sources and degradation of terrestrial organic carbon along the Kolyma paleoriver transect, East Siberian Sea. *Biogeosciences*, *7*(10), 3153–3166. http://doi.org/10.5194/bg-7-3153-2010

Vonk, J. E., Semiletov, I. P., Dudarev, O. V, Eglinton, T. I., Andersson, A., Shakhova, N., … Gustafsson, Ö. (2014). Preferential burial of permafrost-derived organic carbon in Siberian-Arctic shelf waters. *Journal of Geophysical Research: Oceans*, *119*(12), 8410–8421. http://doi.org/10.1002/2014JC010261

Vonk, J. E., Tesi, T., Bröder, L., Holmstrand, H., Hugelius, G., Andersson, A., … Gustafsson, Ö. (2017). Distinguishing between old and modern permafrost sources in the northeast Siberian land-shelf system with compound-specific δ2H analysis. *Cryosphere*, *11*(4), 1879–1895. http://doi.org/10.5194/tc-11-1879-2017

Wacker, L., & Christl, M. (2011). Data reduction for small radiocarbon samples: Error propagation using the model of constant contamination. *Ion Beam Physics, ETH Zurich, Annual Report 2011*, *200*, 36.

Walter, K. M., Zimov, S. A., Chanton, J. P., Verbyla, D., & Chapin, F. S. (2006). Methane bubbling from Siberian thaw lakes as a positive feedback to climate warming. *Nature*, *443*(7107), 71–75. http://doi.org/10.1038/nature05040

Winterfeld, M. (2016). *LENA 2013_cores_160930*.

Yi, Y., Kimball, J. S., Chen, R. H., Moghaddam, M., Reichle, R. H., Mishra, U., … Oechel, W. C. (2018). Characterizing permafrost active layer dynamics and sensitivity to landscape spatial heterogeneity in Alaska. *Cryosphere*, *12*(1), 145–161. http://doi.org/10.5194/tc-12-145-2018

Zhang, T., Barry, R. G., Knowles, K., Ling, F., & Armstrong, R. L. (2003). Distribution of seasonally and perennially frozen ground in the Northern Hemisphere. *Permafrost*, 1289–1294.

Zimov, S., Schuur, E., & Chapin III, F. S. (2006). Permafrost and the global carbon budget. *Science*, *312*(June), 1612–1613.

8 Appendix

Equations:

Appendix Equation 1: Error propagation for Equation (2):

$$\sigma^2_{\delta13C_{smp}} = \left(\frac{n}{n-1} * \sigma_{\delta13C_m}\right)^2 + \left(\frac{-1}{n-1} * \sigma_{\delta13C_{MeOH}}\right)^2 \tag{AE1}$$

Appendix-Equation 2: Error propagation for Equation (3):

$$\sigma^2_{\delta13C_{smp}} = \left(\frac{n}{n-1} * \sigma_{\delta13C_m}\right)^2 + \left(\frac{-1}{n-1} * \sigma_{\delta13C_{MeOH}}\right)^2 \tag{AE2}$$

In order to determine the IRMS analytical error an alkane standard with known isotopic composition was measured periodically after 6 IRMS sample runs, resulting in a long term average analytical error of ± 0.2 ‰. This value was used as the individual measurement error $\sigma_{\delta13C_m}$. If the difference between a single measurement value and the mean value for that sample was > 0.2 ‰, the difference was used as $\sigma_{\delta13C_m}$.

Blank correction

The contribution of the standard and the blank to the measured value can be expressed through a mass balance equation (John M Hayes, 2002; Hwang & Druffel, 2005), where m is the carbon mass and standard and blank are described by subscripts *std* and *b* respectively:

$$fMC_{std+b} * m_{std+b} = fMC_{std} * m_{std} + fMC_b * m_b \tag{AE3}$$

Using $m_b = m_{std+b} - m_{std}$ equation (?) can be changed to:

$$fMC_{std+b} = (fMC_b + fMC_{std}) * m_b * \frac{1}{m_{std+b}} + fMC_{std} \tag{AE4}$$

Under the assumption that fMC_b and m_b are constant and because fMC_{std} is known, (AE4) can be expressed as a linear function $y = m * x + b$ with $(fMC_b + fMC_{std}) * m_b$ as the slope, $1/m_{std+b}$ as the x-variable and fMC_{std} as the y-intercept and correct fMC of the standard.

When samples of two different standards are measured and the resulting fMC_{std+b} are plotted against the respective $1/m_{std+b}$ the intercept (x/y) of the two linear functions defines $1/m_b$ and fMC_b (Hwang & Druffel, 2005).

With $1/m_b$ and fMC_b the measured fMC of a sample (fMC_{smp+b}) can be blank corrected (described by subscript *bc*) using the following equation:

$$fMC_{bc} = \frac{fMC_{smp+b} * m_{smp+b} + fMC_b * m_b}{m_{smp+b} - m_b} \tag{AE5}$$

Error propagation can be used to calculate the squared error $\sigma^2_{fMC_{bc}}$ of fMC_{bc} (changed after Wacker & Christl, 2011), where σ_{m_b}, σ_{fMC_b}, $\sigma_{m_{smp+b}}$ and $\sigma_{fMC_{smp+b}}$ are the individual errors of the subscripted values:

$$\sigma^2_{fMC_{bc}} = \left(\frac{m_{smp+b} * (-fMC_b + fMC_{smp+b})}{(m_{smp+b} - m_b)^2} * \sigma_{m_b}\right)^2 + \left(\frac{-m_b}{m_{smp+b} - m_b} * \sigma_{fMC_b}\right)^2 +$$

$$\left(\frac{m_b * (fMC_b - fMC_{smp+b})}{\left(m_{smp+b} - m_b\right)^2} * \sigma_{m_{smp+b}}\right)^2 + \left(\frac{m_{smp+b}}{m_{smp+b} - m_b} * \sigma_{fMC_{smp+b}}\right)^2 \quad \text{(AE6)}$$

Methyl correction:

The fMC_{bc} composes proportionally of the true fMC of the sample (fMC_{smp}) and the fMC of the MeOH (fMC_{MeOH}) used for methylation, as shown by the following mass balance equation:

$$fMC_{bc} = \frac{1}{n} * fMC_{MeOH} + \frac{n-1}{n} * fMC_{smp} \quad \text{(AE7)}$$

Equation (9) can be rearranged to conduct the methyl correction and calculate fMC_{smp}, where n is the total number of carbon atoms in the molecule after methylation:

$$fMC_{smp} = \left(fMC_{bc} - \frac{1}{n} * fMC_{MeOH}\right) * \frac{n}{n-1}$$

Error propagation yields the respective error $\sigma_{fMC_{smp}}$:

$$\sigma^2_{fMC_{smp}} = \left(\frac{n}{n-1} * \sigma_{fMC_{bc}}\right)^2 + \left(\frac{-1}{n-1} * \sigma_{fMC_{MeOH}}\right)^2 \quad \text{(AE8)}$$

Blank correction of the studied samples was conducted using two different processing standards, one isotopically dead (Messel Shale, $fMC_{MS} = 0$) and one with a modern radiocarbon content (Apple Peel, $fMC_{AP} = 1.0311$). Samples of the standards were extracted and processed in the same way as sedimentary samples. FAMEs of the standard samples were separated according to chain length using Prep-GC and the split weights were converted into µgC depending on the individual carbon chain length. 8 Messel Shale samples with chain length from 24 to 30 carbon atoms and 9 Apple Peel samples with chain length of 16, 26 and 28 carbon atoms were measured. In order to plot the results as a linear function, ranges of different sample weights (Messel Shale: 12-52 µgC; Apple Peel 3-71 µgC) were measured.

Analysis was conducted using the MICADAS system connected to the EA using the settings described in 2.4.3. The resulting data and respective errors were plotted against the inverted sample weight (Appendix-Figure 2). Since the standards are FAMEs, the fMC was calculated for each measured FAME C chain length according to equation (9), in which case fMC_{smp} is fMC of the initial standard. The true fMC was then calculated as a weighted mean of all measurements (Appendix-Table 2). A linear regression line was applied for each standard with the weighted mean as the set y-intercept.

	fMC initial	FAME C chain length	fMC FAME (weighted mean)
Apple Peel	1.0311 ± 0.0038	$C_{16:0}$, $C_{26:0}$, $C_{28:0}$	$2.9 * 10^{-5}$
Messel Shale	0	$C_{24:0}$ - $C_{30:0}$	0.9838

Appendix Table 1: Summary of the used standards with initial fMC (Mollenhauer, unpublished) and calculated weighted mean fMC of the standard FAMEs.
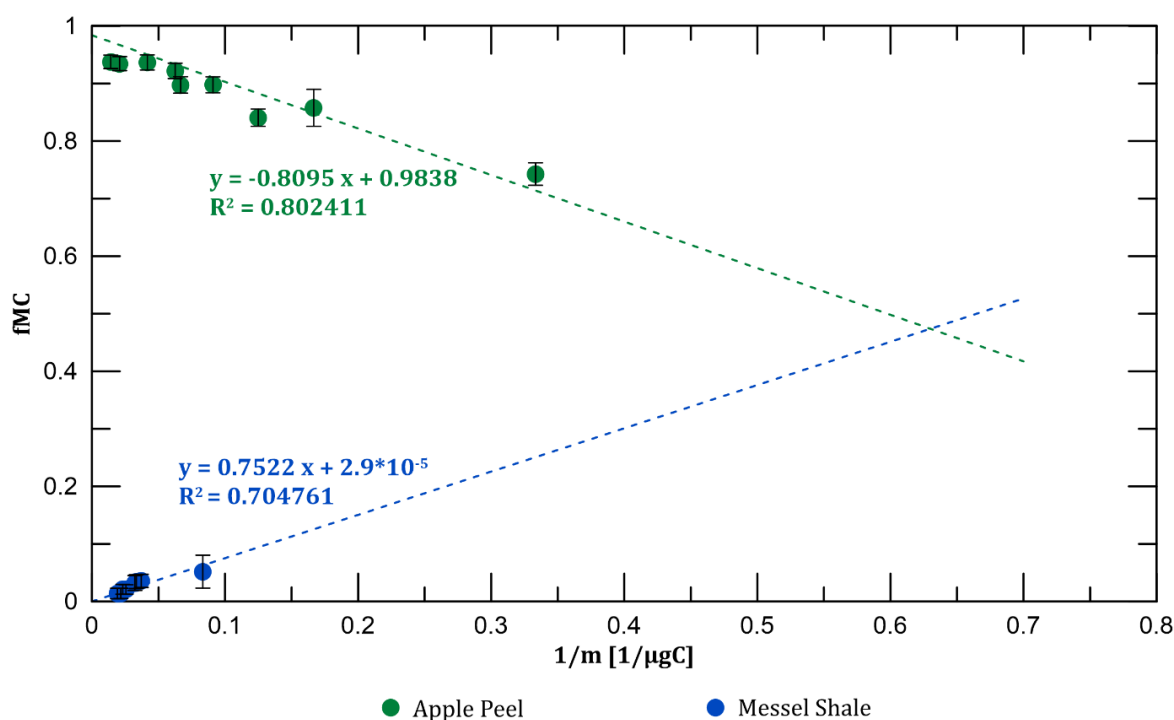
Appendix Figure 1: Results of the standard measurements plotted against the inverted mass of contained C. Individual errors of f14C values are shown, for visibility Messel Shale errors are amplified by a factor of 10. Linear regression lines (dashed lines) for each standard are shown with the respective equation and correlation factor R².

Setting the linear regression functions equal yield the intercept (x/y) = (0.6300/0.4739) and the blank properties $m_b = 1.59\ \mu gC$ and $fMC_b = 0.4739$ were determined. Due to the weaker correlation of the Messel Shale regression line, the error σ_{fMC_b} was calculated as follows:

$$\sigma_{fMC_b} = fMC_b * (1 - R^2_{MS}) = 0.4739 * 0.7048 = 0.1399 \qquad \text{(AE9)}$$

sample	sample weight [g]	TOC [wt%]	TOC/sample [g]
0-1cm	3.00	1.77	0.053
1-2cm	3.00	1.55	0.046
2-3cm	3.00	1.50	0.045
3-4cm	3.03	1.64	0.050
4-5cm	3.01	1.54	0.046
5-6cm	3.04	1.31	0.040
6-7cm	2.80	1.50	0.042
7-8cm	3.00	1.53	0.046
8-9cm	3.00	1.68	0.050
9-10cm	3.01	1.47	0.044
10-11cm	3.00	1.52	0.046
11-12cm	3.02	1.43	0.043
12-13cm	3.00	1.51	0.045
13-14cm	2.99	1.51	0.045
14-15cm	3.01	1.48	0.045
15-16cm	3.00	1.67	0.050
16-17cm	3.01	1.42	0.043
17-18cm	3.01	1.33	0.040
18-19cm	3.01	1.33	0.040
19-20cm	3.00	1.43	0.043
20-21cm	3.03	1.42	0.043
21-22cm	3.00	1.36	0.041
22-23cm	3.00	1.35	0.041
23-24cm	3.02	1.39	0.042

Appendix Table 2: Sample characteristics for core L13-04-2.

sample	sample weight [g]	TOC [wt%]	TOC/sample [g]
0-1cm	3.00	1.75	0.053
1-3cm	3.00	1.99	0.060
3-5cm	3.00	1.95	0.058
5-7cm	3.00	1.69	0.051
7-9cm	3.00	1.96	0.059
9-11cm	3.01	1.97	0.059
11-13cm	3.00	1.91	0.057
13-15cm	3.00	1.84	0.055
15-17cm	3.00	2.07	0.062
17-19cm	3.01	1.91	0.058
19-21cm	3.00	2.05	0.061
21-23cm	3.00	1.52	0.046
23-25cm	3.00	1.83	0.055

Appendix Table 3: Sample characteristics for core L13-18-2.

sample	$C_{16:0}$	$C_{18:0}$	$C_{20:0}$	ISTD	$C_{22:0}$	$C_{23:0}$	$C_{24:0}$	$C_{25:0}$	$C_{26:0}$	$C_{27:0}$	$C_{28:0}$	$C_{29:0}$	$C_{30:0}$	$\sum C_{21} - C_{33}$
0-1cm	69.950	8.609	12.793	16.104	23.322	8.612	29.140	6.755	16.689	3.594	9.635	1.429	3.603	40.886
1-2cm	58.684	7.212	11.278	16.104	20.846	7.652	26.310	5.998	14.772	3.047	8.100	1.137	2.794	36.109
2-3cm	35.314	6.575	10.621	16.104	19.959	7.291	25.436	5.769	14.331	2.789	7.012	0.913	2.133	33.342
3-4cm	39.464	7.679	13.335	16.104	25.177	9.313	32.468	7.026	17.483	3.292	8.543	1.121	2.742	36.242
4-5cm	19.088	5.850	10.369	16.104	21.112	8.141	30.472	7.371	20.794	4.569	13.531	1.961	4.995	30.213
5-6cm	12.425	4.305	7.545	16.104	15.111	5.767	21.514	5.182	14.641	3.242	9.538	1.380	3.448	23.492
6-7cm	11.276	4.444	7.984	16.104	15.981	6.348	23.465	5.757	16.324	3.708	11.330	1.757	4.808	23.351
7-8cm	16.546	5.737	9.950	16.104	19.052	7.104	25.417	5.742	14.401	2.812	7.438	1.002	2.416	28.918
8-9cm	15.192	5.480	9.454	16.104	17.679	6.532	23.260	5.097	13.133	2.615	7.123	0.974	2.375	27.562
9-10cm	13.598	5.269	9.256	16.104	17.788	6.617	23.781	5.299	13.877	2.730	7.285	0.976	2.359	26.474
10-11cm	12.485	4.945	8.604	16.104	16.561	6.083	21.632	4.781	12.183	2.449	6.521	0.000	2.161	26.346
11-12cm	11.106	4.937	8.759	16.104	16.427	5.984	22.398	5.124	14.843	3.237	9.855	0.000	3.669	25.836
12-13cm	12.547	5.402	10.017	16.104	20.071	7.414	29.128	6.841	19.601	4.292	12.972	1.893	5.032	30.533
13-14cm	11.242	5.062	9.499	16.104	18.812	6.976	27.569	6.445	18.646	4.074	12.095	1.735	4.550	28.744
14-15cm	11.701	5.301	9.580	16.104	18.573	6.820	25.572	5.756	16.184	3.477	10.574	1.576	4.325	27.527
15-16cm	10.994	4.777	8.631	16.104	17.391	6.452	25.077	5.727	16.333	3.510	10.886	1.624	4.509	24.859
16-17cm	9.857	4.515	8.344	16.104	17.365	6.668	25.850	5.950	17.076	3.701	11.179	1.634	4.451	23.431
17-18cm	9.317	4.432	8.020	16.104	16.239	6.190	24.122	5.568	16.120	3.485	10.561	1.525	4.124	23.035
18-19cm	9.372	4.388	7.947	16.104	15.860	5.959	23.068	5.403	15.463	3.364	10.260	1.519	4.123	23.001
19-20cm	9.253	4.528	8.165	16.104	16.342	6.349	25.292	6.116	17.860	4.018	12.220	1.857	5.020	24.588
20-21cm	6.381	3.301	5.911	16.104	11.178	3.938	15.506	3.494	9.903	2.101	6.247	0.000	2.392	17.020
21-22cm	9.138	4.729	7.971	16.104	14.500	5.315	20.083	4.624	12.978	2.847	8.514	0.000	3.510	22.610
22-23cm	8.672	4.496	7.884	16.104	14.679	5.547	21.517	5.135	14.527	3.204	9.697	1.473	3.914	23.979
23-24cm	8.746	4.468	7.186	16.104	12.762	4.476	17.341	3.970	10.890	2.314	6.702	0.000	2.517	24.551

Appendix Table 4: Concentrations of *n*-alcanoic acids in core L13-04-2 [μg]

sample	C_{21}	C_{22}	C_{23}	C_{24}	C_{25}	C_{26}	(IS)	C_{27}	C_{28}	C_{29}	C_{30}	C_{31}	C_{32}	C_{33}	$\sum C_{21}$- C_{33}
0-1cm	1.730	1.914	3.773	1.568	4.453	1.413	8.2	8.129	1.221	7.176	0.689	6.384	0.35	2.086	0.079
1-2cm	1.528	1.471	3.334	1.378	3.895	1.257	8.2	7.212	1.079	6.399	0.612	5.732	0.319	1.893	0.071
2-3cm	1.420	1.462	3.116	1.284	3.695	1.149	8.2	6.644	0.995	5.865	0.564	5.171	0.29	1.687	0.063
3-4cm	1.568	1.522	3.403	1.398	3.890	1.273	8.2	7.201	1.110	6.361	0.64	5.679	0.323	1.874	0.077
4-5cm	1.270	1.281	2.820	1.168	3.270	1.042	8.2	5.982	0.903	5.34	0.507	4.795	0.263	1.572	0.073
5-6cm	0.955	0.949	2.133	0.911	2.504	0.793	8.2	4.681	0.700	4.231	0.393	3.771	0.214	1.257	0.044
6-7cm	1.003	1.007	2.224	0.928	2.571	0.822	8.2	4.705	0.708	4.107	0.39	3.55	0.196	1.140	0.057
7-8cm	1.234	1.271	2.648	1.118	3.087	1.010	8.2	5.726	0.884	5.083	0.513	4.555	0.264	1.525	0.061
8-9cm	1.158	1.228	2.508	1.054	2.927	0.961	8.2	5.452	0.844	4.871	0.489	4.363	0.251	1.456	0.059
9-10cm	1.108	1.187	2.43	1.018	2.839	0.943	8.2	5.267	0.815	4.634	0.478	4.136	0.241	1.378	0.057
10-11cm	1.130	1.238	2.424	1.025	2.826	0.937	8.2	5.219	0.809	4.615	0.471	4.06	0.237	1.355	0.055
11-12cm	1.043	1.018	2.325	0.974	2.779	0.889	8.2	5.182	0.788	4.627	0.445	4.144	0.232	1.390	0.061
12-13cm	1.247	1.237	2.793	1.160	3.301	1.043	8.2	6.109	0.925	5.447	0.520	4.864	0.272	1.615	0.079
13-14cm	1.171	1.156	2.606	1.093	3.110	1.014	8.2	5.756	0.872	5.118	0.495	4.563	0.258	1.532	0.073
14-15cm	1.147	1.111	2.560	1.063	2.999	0.965	8.2	5.509	0.842	4.854	0.473	4.319	0.243	1.442	0.066
15-16cm	1.035	1.106	2.299	0.954	2.696	0.857	8.2	4.947	0.754	4.358	0.429	3.904	0.22	1.300	0.057
16-17cm	1.010	1.026	2.208	0.906	2.561	0.818	8.2	4.667	0.713	4.093	0.402	3.616	0.206	1.205	0.066
17-18cm	0.970	0.992	2.144	0.885	2.510	0.805	8.2	4.601	0.704	4.048	0.398	3.587	0.204	1.187	0.056
18-19cm	0.971	0.959	2.128	0.890	2.486	0.803	8.2	4.604	0.702	4.056	0.398	3.592	0.206	1.206	0.051
19-20cm	1.026	1.051	2.285	0.959	2.663	0.853	8.2	4.899	0.752	4.336	0.465	3.811	0.217	1.271	0.061
20-21cm	0.705	0.736	1.595	0.685	1.878	0.608	8.2	3.426	0.526	2.981	0.293	2.596	0.144	0.847	0.040
21-22cm	0.927	1.025	2.136	0.903	2.520	0.804	8.2	4.624	0.698	3.954	0.379	3.359	0.190	1.091	0.065
22-23cm	0.944	0.966	2.203	0.934	2.625	0.859	8.2	4.901	0.743	4.275	0.412	3.696	0.209	1.212	0.059
23-24cm	0.953	1.124	2.235	0.949	2.641	0.863	8.2	4.994	0.736	4.349	0.445	3.799	0.211	1.252	0.053

Appendix Table 5: Concentrations of *n*-alkanes in core L13-04-2 [µg]

sample	$C_{16:0}$	$C_{18:0}$	$C_{20:0}$	ISTD	$C_{22:0}$	$C_{23:0}$	$C_{24:0}$	$C_{25:0}$	$C_{26:0}$	$C_{27:0}$	$C_{28:0}$	$C_{29:0}$	$C_{30:0}$	$\sum C_{21}$-C_{33}
0-1cm	79.100	14.829	13.249	16.104	4.212	29.447	11.006	40.544	8.194	22.672	4.464	13.643	1.852	137.026
1-3cm	31.548	9.157	13.594	16.104	4.043	27.603	9.578	34.463	6.572	18.416	3.488	11.607	1.620	118.219
3-5cm	21.875	7.430	13.355	16.104	4.037	27.993	9.918	36.976	7.119	20.271	3.869	12.870	1.793	126.261
5-7cm	16.910	6.223	10.338	16.104	3.087	21.128	7.234	27.572	5.336	15.076	2.918	9.170	0.000	91.796
7-9cm	14.963	5.679	9.293	16.104	2.650	19.056	6.159	24.746	4.787	13.830	2.646	8.641	0.000	83.130
9-11cm	17.147	6.843	12.544	16.104	3.632	27.414	9.384	35.590	6.307	17.795	3.156	10.405	1.365	115.609
11-13cm	17.115	6.938	13.230	16.104	3.865	29.118	10.135	38.017	6.800	19.225	3.461	11.542	1.541	124.705
13-15cm	16.651	6.514	11.116	16.104	3.078	22.659	7.359	29.552	5.493	16.399	3.058	10.256	0.000	98.689
15-17cm	18.146	7.033	13.238	16.104	3.736	27.860	9.218	37.455	7.085	21.119	3.940	12.857	1.657	126.032
17-19cm	15.864	6.831	12.882	16.104	3.733	26.905	9.290	34.946	6.334	18.058	3.294	10.970	1.480	115.971
19-21cm	16.935	7.358	13.954	16.104	4.192	30.508	10.884	41.323	7.613	21.500	3.881	12.826	1.736	135.607
21-23cm	14.192	6.192	11.815	16.104	3.608	26.123	9.012	34.631	6.525	18.681	3.498	11.611	1.572	116.463
23-25cm	12.827	5.516	9.187	16.104	2.540	18.085	5.653	23.364	4.458	13.321	2.597	8.624	0.000	79.592

Appendix Table 6: Concentrations of *n*-alcanoic acids in core L13-018-2 [µg]

sample	C_{21}	C_{22}	C_{23}	C_{24}	C_{25}	C_{26}	(IS)	C_{27}	C_{28}	C_{29}	C_{30}	C_{31}	C_{32}	C_{33}	$\sum C_{21}$-C_{33}
0-1cm	1.374	1.181	3.254	1.257	4.101	1.233	8.2	8.276	1.206	6.954	0.628	5.993	0.361	1.910	37.728
1-3cm	1.366	1.133	3.183	1.192	3.905	1.156	8.2	7.857	1.019	6.625	0.591	5.666	0.315	1.818	35.826
3-5cm	1.296	1.058	3.040	1.136	3.710	1.074	8.2	7.440	0.983	6.103	0.549	5.096	0.283	1.627	33.395
5-7cm	0.977	0.820	2.284	0.869	2.893	0.856	8.2	5.897	0.764	4.967	0.432	4.232	0.242	1.381	26.614
7-9cm	0.851	0.680	2.049	0.781	2.640	0.769	8.2	5.509	0.690	4.59	0.386	3.855	0.219	1.246	24.265
9-11cm	1.103	0.896	2.580	0.969	3.289	0.933	8.2	6.846	0.915	5.585	0.481	4.538	0.261	1.461	29.857
11-13cm	1.128	0.917	2.685	1.004	3.407	0.963	8.2	7.113	0.878	5.654	0.487	4.626	0.256	1.468	30.586
13-15cm	0.967	0.818	2.329	0.883	3.038	0.871	8.2	6.437	0.792	5.320	0.442	4.424	0.249	1.432	28.002
15-17cm	1.145	0.965	2.722	1.054	3.510	0.998	8.2	7.303	0.924	6.101	0.512	5.183	0.287	1.689	32.393
17-19cm	1.185	0.955	2.803	1.036	3.515	1.008	8.2	6.925	0.876	5.500	0.503	4.670	0.263	1.488	30.727
19-21cm	1.295	1.088	3.091	1.152	3.934	1.108	8.2	7.870	1.016	6.258	0.569	5.246	0.301	1.695	34.623
21-23cm	1.065	0.872	2.535	0.977	3.236	0.959	8.2	6.570	0.838	5.387	0.485	4.392	0.260	1.415	28.991
23-25cm	0.921	0.778	2.216	0.862	2.899	0.840	8.2	5.950	0.771	4.954	0.425	4.155	0.240	1.363	26.374

Appendix Table 7: Concentrations of n-alkanes in core L13-18-2 [µg]

sample	YOS	error YOS ±	MAR [(g/cm²)/a]	error MAR ±
0-1cm	2012.2	2.2	0.045	0.003
1-2cm	2009.8	2.2	0.039	0.003
2-3cm	2006.8	2.2	0.043	0.003
3-4cm	2003.3	2.3	0.038	0.003
4-5cm	1998.8	2.4	0.033	0.003
5-6cm	1993.8	2.6	0.042	0.004
6-7cm	1989.8	2.7	0.051	0.005
7-8cm	1984.8	3.0	0.027	0.003
8-9cm	1978.1	3.4	0.026	0.004
9-10cm	1971.7	3.8	0.031	0.005
10-11cm	1964.8	4.4	0.025	0.005
11-12cm	1959.4	4.6	0.074	0.021
12-13cm	1953.4	5.5	0.023	0.006
13-14cm	1946.2	6.3	0.040	0.012
14-15cm	1928.9	12.4	0.008	0.005
15-16cm	1912.8	13.2	0.059	0.050
16-17cm	1910.8	13.2	0.379	0.871
17-18cm	1907.2	14.1	0.033	0.032
18-19cm	1901.0	14.8	0.039	0.048
19-20cm	1897.3	14.8	0.148	0.263
20-21cm	1896.5	14.3		
21-22cm	1888.1	16.6		
22-23cm	1879.6	16.6		
23-24cm	1862.5	32.1		

Appendix Table 8: CRS-model of core L13-04-2 (Pittauer, 2018; unpublished): *Year of sedimentation (YOS) and mass accumulation rate (MAR) with respective errors.*

sample	YOS	error YOS ±	MAR [(g/cm²)/a]	error MAR ±
0-1cm	2011.8	2.8	0.071	0.005
1-3cm	2008.2	2.9	0.071	0.005
3-5cm	2002.8	3.1	0.065	0.005
5-7cm	1996.6	3.4	0.068	0.007
7-9cm	1990.6	3.8	0.086	0.007
9-11cm	1985.1	4.2	0.084	0.009
11-13cm	1977.6	5.0	0.056	0.008
13-15cm	1969.8	6.0	0.079	0.014
15-17cm	1964.0	6.8	0.101	0.023
17-19cm	1959.1	7.7	0.099	0.021
19-21cm	1951.7	9.4	0.052	0.014
21-23cm	1941.5	12.4	0.054	0.020
23-25cm	1933.1	15.5	0.041	0.021

Appendix Table 9: CRS-model of core L13-18-2 (Pittauer, 2018; unpublished): *Year of sedimentation (YOS) and mass accumulation rate (MAR) with respective errors.*

sample	C-chain length	fMC	fMC ±	weight (µg)
L13-04-2, surface	C16:0-FAME	0.7952	0.0100	81
L13-04-2, surface	C18:0-FAME	0.5718	0.0079	46
L13-04-2, surface	C22:0-FAME	0.5096	0.0073	126
L13-04-2, surface	C24:0-FAME	0.4689	0.0068	129
L13-04-2, surface	C26:0-FAME	0.4407	0.0067	129
L13-04-2, surface	C28:0-FAME	0.4375	0.0059	91
L13-04-2, 4-7 cm	C16:0-FAME	0.7850	0.0098	56
L13-04-2, 4-7 cm	C18:0-FAME	0.7001	0.0094	72
L13-04-2, 4-7 cm	C22:0-FAME	0.5282	0.0077	125
L13-04-2, 4-7 cm	C24:0-FAME	0.4756	0.0068	113
L13-04-2, 4-7 cm	C26:0-FAME	0.4380	0.0063	131
L13-04-2, 4-7 cm	C28:0-FAME	0.4449	0.0061	152
L13-04-2, 12-15 cm	C16:0-FAME	0.7185	0.0090	74
L13-04-2, 12-15 cm	C18:0-FAME	0.6958	0.0095	51
L13-04-2, 12-15 cm	C22:0-FAME	0.5159	0.0075	148
L13-04-2, 12-15 cm	C24:0-FAME	0.4768	0.0067	132
L13-04-2, 12-15 cm	C26:0-FAME	0.4342	0.0063	127
L13-04-2, 12-15 cm	C28:0-FAME	0.4404	0.0063	75
L13-04-2, 17-20 cm	C16:0-FAME	0.5974	0.0078	51
L13-04-2, 17-20 cm	C18:0-FAME	0.5534	0.0078	55
L13-04-2, 17-20 cm	C22:0-FAME	0.4812	0.0069	44
L13-04-2, 17-20 cm	C24:0-FAME	0.4442	0.0063	73
L13-04-2, 17-20 cm	C24:0-FAME	0.4450	0.0065	67
L13-04-2, 17-20 cm	C24:0-FAME	0.4471	0.0060	48
L13-04-2, 17-20 cm	C24:0-FAME	0.4512	0.0062	38
L13-04-2, 17-20 cm	C24:0-FAME	0.4449	0.0071	27
L13-04-2, 17-20 cm	C26:0-FAME	0.4240	0.0061	39
L13-04-2, 17-20 cm	C28:0-FAME	0.4186	0.0059	48
L13-04-2, 21-23 cm	C16:0-FAME	0.5814	0.0076	58
L13-04-2, 21-23 cm	C18:0-FAME	0.5016	0.0071	32
L13-04-2, 21-23 cm	C22:0-FAME	0.4652	0.0070	32
L13-04-2, 21-23 cm	C24:0-FAME	0.4500	0.0067	99
L13-04-2, 21-23 cm	C26:0-FAME	0.4259	0.0063	88
L13-04-2, 21-23 cm	C28:0-FAME	0.4134	0.0058	111

Appendix Table 10: CRSA results of core L13-04-2.

sample	C-chain length	$\Delta^{14}C_{initial}$	$\Delta^{14}C_{initial}$ ±	Age [years]
L13-04-2, surface	C16:0-FAME	-147.761	1.7	1328
L13-04-2, surface	C18:0-FAME	-392.409	5.1	4125
L13-04-2, surface	C22:0-FAME	-466.435	6.4	5199
L13-04-2, surface	C24:0-FAME	-511.318	7.1	5925
L13-04-2, surface	C26:0-FAME	-542.492	8.0	6470
L13-04-2, surface	C28:0-FAME	-547.280	7.1	6557
L13-04-2, 4-7 cm	C16:0-FAME	-153.927	1.8	1406
L13-04-2, 4-7 cm	C18:0-FAME	-253.567	3.3	2441
L13-04-2, 4-7 cm	C22:0-FAME	-445.514	6.2	4899
L13-04-2, 4-7 cm	C24:0-FAME	-503.148	6.9	5806
L13-04-2, 4-7 cm	C26:0-FAME	-544.325	7.6	6521
L13-04-2, 4-7 cm	C28:0-FAME	-538.236	7.1	6412
L13-04-2, 12-15 cm	C16:0-FAME	-223.965	2.7	2171
L13-04-2, 12-15 cm	C18:0-FAME	-251.263	3.4	2467
L13-04-2, 12-15 cm	C22:0-FAME	-455.264	6.4	5097
L13-04-2, 12-15 cm	C24:0-FAME	-498.789	6.9	5785
L13-04-2, 12-15 cm	C26:0-FAME	-545.491	7.8	6594
L13-04-2, 12-15 cm	C28:0-FAME	-540.440	7.6	6502
L13-04-2, 17-20 cm	C16:0-FAME	-352.018	4.5	3703
L13-04-2, 17-20 cm	C18:0-FAME	-405.140	5.6	4410
L13-04-2, 17-20 cm	C22:0-FAME	-489.582	6.9	5676
L13-04-2, 17-20 cm	C24:0-FAME	-524.085	7.5	6348
L13-04-2, 17-20 cm	C24:0-FAME	-555.716	8.0	6823
L13-04-2, 17-20 cm	C24:0-FAME	-565.766	7.9	6947
L13-04-2, 17-20 cm	C24:0-FAME	-368.952	4.7	3940
L13-04-2, 17-20 cm	C24:0-FAME	-460.330	6.4	5233
L13-04-2, 17-20 cm	C26:0-FAME	-506.223	7.5	5968
L13-04-2, 17-20 cm	C28:0-FAME	-524.005	7.7	6271
L13-04-2, 21-23 cm	C16:0-FAME	-551.409	8.0	6761
L13-04-2, 21-23 cm	C18:0-FAME	-147.761	1.7	1328
L13-04-2, 21-23 cm	C22:0-FAME	-392.409	5.1	4125
L13-04-2, 21-23 cm	C24:0-FAME	-466.435	6.4	5199
L13-04-2, 21-23 cm	C26:0-FAME	-511.318	7.1	5925
L13-04-2, 21-23 cm	C28:0-FAME	-542.492	8.0	6470

Appendix Table 11: Calculated $\Delta^{14}C_{initial}$ values and ages of core L13-04-2.

sample	C-chain length	fMC	fMC ±	weight (µg)
L13-18-2, surface	C16:0-FAME	0.7549	0.0095	77
L13-18-2, surface	C18:0-FAME	0.4759	0.0068	35
L13-18-2, surface	C22:0-FAME	0.5656	0.0081	95
L13-18-2, surface	C24:0-FAME	0.5349	0.0077	90
L13-18-2, surface	C26:0-FAME	0.4922	0.0068	88
L13-18-2, surface	C28:0-FAME	0.4870	0.0064	94
L13-18-2, 5-9 cm	C16:0-FAME	0.6938	0.0088	43
L13-18-2, 5-9 cm	C18:0-FAME	0.6004	0.0084	69
L13-18-2, 5-9 cm	C22:0-FAME	0.5696	0.0082	89
L13-18-2, 5-9 cm	C24:0-FAME	0.5334	0.0076	93
L13-18-2, 5-9 cm	C26:0-FAME	0.5008	0.0071	65
L13-18-2, 5-9 cm	C28:0-FAME	0.4848	0.0068	163
L13-18-2, 13-17 cm	C16:0-FAME	0.6570	0.0086	147
L13-18-2, 13-17 cm	C18:0-FAME	0.5860	0.0084	72
L13-18-2, 13-17 cm	C22:0-FAME	0.5549	0.0077	86
L13-18-2, 13-17 cm	C24:0-FAME	0.5425	0.0078	84
L13-18-2, 13-17 cm	C26:0-FAME	0.5040	0.0072	96
L13-18-2, 13-17 cm	C28:0-FAME	0.5009	0.0071	130
L13-18-2, 21-24 cm	C16:0-FAME	0.6220	0.0083	122
L13-18-2, 21-24 cm	C18:0-FAME	0.5725	0.0086	71
L13-18-2, 21-24 cm	C22:0-FAME	0.5523	0.0083	83
L13-18-2, 21-24 cm	C24:0-FAME	0.5304	0.0079	80
L13-18-2, 21-24 cm	C26:0-FAME	0.4908	0.0070	81
L13-18-2, 21-24 cm	C28:0-FAME	0.4982	0.0070	119

Appendix Table 12: CRSA results of core L13-04-2.

sample	C-chain length	$\Delta^{14}C_{initial}$	$\Delta^{14}C_{initial}$ ±	Age [years]
L13-18-2, surface	C16:0-FAME	-191.123	2.3	1760
L13-18-2, surface	C18:0-FAME	-497.250	6.7	5691
L13-18-2, surface	C22:0-FAME	-406.691	5.6	4322
L13-18-2, surface	C24:0-FAME	-441.255	6.1	4818
L13-18-2, surface	C26:0-FAME	-488.120	6.5	5542
L13-18-2, surface	C28:0-FAME	-494.986	6.3	5654
L13-18-2, 5-9 cm	C16:0-FAME	-251.703	3.0	2421
L13-18-2, 5-9 cm	C18:0-FAME	-361.248	4.8	3730
L13-18-2, 5-9 cm	C22:0-FAME	-400.987	5.6	4261
L13-18-2, 5-9 cm	C24:0-FAME	-441.703	6.1	4843
L13-18-2, 5-9 cm	C26:0-FAME	-477.773	6.5	5395
L13-18-2, 5-9 cm	C28:0-FAME	-496.367	6.8	5695
L13-18-2, 13-17 cm	C16:0-FAME	-295.493	3.7	2947
L13-18-2, 13-17 cm	C18:0-FAME	-374.940	5.2	3936
L13-18-2, 13-17 cm	C22:0-FAME	-414.699	5.6	4479
L13-18-2, 13-17 cm	C24:0-FAME	-430.039	6.0	4699
L13-18-2, 13-17 cm	C26:0-FAME	-472.888	6.6	5345
L13-18-2, 13-17 cm	C28:0-FAME	-477.690	6.6	5420
L13-18-2, 21-24 cm	C16:0-FAME	-330.9673	4.3	3399
L13-18-2, 21-24 cm	C18:0-FAME	-387.672	5.6	4131
L13-18-2, 21-24 cm	C22:0-FAME	-415.618	6.1	4517
L13-18-2, 21-24 cm	C24:0-FAME	-441.243	6.4	4888
L13-18-2, 21-24 cm	C26:0-FAME	-485.311	6.8	5567
L13-18-2, 21-24 cm	C28:0-FAME	-478.878	6.6	5464

Appendix Table 13: Calculated $\Delta^{14}C_{initial}$ values and ages of core L13-18-2.

sample	$\delta^{13}C\ C_{16:0}$	$\sigma\ \delta^{13}C\ C_{16:0}$	$\delta^{13}C\ C_{28:0}$	$\sigma\ \delta^{13}C\ C_{28:0}$
0-1cm	-21.48	0.21	-33.06	0.24
1-2cm	-22.15	0.23	-33.17	0.21
2-3cm	-25.48	0.21	-33.27	0.21
3-4cm	-26.54	0.24	-33.17	0.21
4-5cm	-29.02	0.21	-32.99	0.33
5-6cm	-30.29	0.21	-33.27	0.21
6-7cm	-30.89	0.21	-32.85	0.21
7-8cm	-30.61	0.21	-33.00	0.21
8-9cm	-31.33	0.22	-33.16	0.21
9-10cm	-31.31	0.21	-33.10	0.21
10-11cm	-31.10	0.21	-32.90	0.21
11-12cm	-31.57	0.21	-32.79	0.21
12-13cm	-31.55	0.21	-32.63	0.21
13-14cm	-31.94	0.21	-33.08	0.21
14-15cm	-31.88	0.21	-32.91	0.21
15-16cm	-31.76	0.21	-32.96	0.21
16-17cm	-31.71	0.21	-32.84	0.21
17-18cm	-31.85	0.27	-32.75	0.26
18-19cm	-31.95	0.21	-33.63	0.21
19-20cm	-31.79	0.21	-32.89	0.21
20-21cm	-32.29	0.21	-32.84	0.21
21-22cm	-32.18	0.21	-33.08	0.21
22-23cm	-32.45	0.28	-32.95	0.21
23-24cm	-31.80	0.21	-33.02	0.21

Appendix Table 14: Stable carbon isotope ratios in core L13-04-2.

sample	$\delta^{13}C\ C_{16:0}$	$\sigma\ \delta^{13}C\ C_{16:0}$	$\delta^{13}C\ C_{28:0}$	$\sigma\ \delta^{13}C\ C_{28:0}$
0-1cm	-25.10	0.21	-33.06	0.21
1-3cm	-29.03	0.21	-32.90	0.21
3-5cm	-31.31	0.21	-32.92	0.21
5-7cm	-31.58	0.21	-32.84	0.21
7-9cm	-31.60	0.21	-32.82	0.27
9-11cm	-31.91	0.21	-32.67	0.21
11-13cm	-31.81	0.21	-32.54	0.21
13-15cm	-31.86	0.21	-32.66	0.21
15-17cm	-31.92	0.21	-32.49	0.21
17-19cm	-31.77	0.21	-32.50	0.21
19-21cm	-31.16	0.21	-32.46	0.21
21-23cm	-31.69	0.21	-32.79	0.27
23-25cm	-32.11	0.21	-32.74	0.28

Appendix Table 15: Stable carbon isotope ratios in core L13-18-2.

sample	$\delta^2H\ C_{16:0}$	$\sigma\ \delta^2H\ C_{16:0}$	$\delta^2H\ C_{28:0}$	$\sigma\ \delta^2H\ C_{28:0}$
0-1cm	-336.10	2.20	-215.52	2.11
1-2cm	-337.24	2.20	-225.00	2.85
2-3cm	-308.58	2.20	-224.77	2.11
3-4cm	-309.97	2.20	-231.05	2.11
4-5cm	-277.64	2.20	-238.47	2.11
5-6cm	-267.13	2.20	-235.21	2.11
6-7cm	-255.46	2.20	-238.80	2.11
7-8cm	-260.02	2.20	-229.11	2.11
8-9cm	-255.72	2.20	-229.88	2.11
9-10cm	-251.00	2.20	-228.70	2.11
10-11cm	-251.28	2.20	-229.32	2.11
11-12cm	-243.33	2.20	-230.20	2.11
12-13cm	-246.19	2.21	-232.51	2.12
13-14cm	-245.86	2.21	-237.80	2.12
14-15cm	-246.65	2.21	-237.66	2.12
15-16cm	-245.64	2.21	-236.67	2.12
16-17cm	-242.82	2.21	-238.11	2.12
17-18cm	-240.92	2.21	-237.75	2.12
18-19cm	-241.85	2.21	-236.14	2.12
19-20cm	-245.23	2.21	-239.64	2.12
20-21cm	-240.15	2.20	-229.76	2.11
21-22cm	-239.82	2.20	-236.19	2.11
22-23cm	-239.06	2.20	-238.68	2.11
23-24cm	-233.80	2.20	-227.22	2.11

Appendix Table 15: Stable hydrogen isotope ratios in core L13-04-2.

sample	$\delta^2H\ C_{16:0}$	$\sigma\ \delta^2H\ C_{16:0}$	$\delta^2H\ C_{28:0}$	$\sigma\ \delta^2H\ C_{28:0}$
0-1cm	-330.2	0.19	-225.85	2.11
1-3cm	-283.0	0.19	-232.70	2.11
3-5cm	-252.8	0.19	-238.88	2.11
5-7cm	-247.3	0.19	-233.30	2.11
7-9cm	-244.6	0.19	-234.95	2.11
9-11cm	-247.6	0.19	-238.97	2.11
11-13cm	-237.2	0.19	-236.45	2.11
13-15cm	-240.8	0.19	-234.99	2.11
15-17cm	-233.3	0.19	-224.66	2.11
17-19cm	-242.6	0.19	-236.46	2.11
19-21cm	-248.7	0.19	-235.00	2.11
21-23cm	-245.4	0.19	-237.54	2.11
23-25cm	-237.6	0.19	-232.56	2.11

Appendix Table 16: Stable hydrogen isotope ratios in core L13-18-2.

sample	Brassicasterol	β-Sitosterol	dinosterol	β-sit/(b-sit+brass+dino)
0-1cm		n.d.		
1-2cm	1.99	5.40	1.39	0.61
2-3cm	2.39	6.04	1.62	0.60
3-4cm	2.06	6.39	1.46	0.64
4-5cm	1.31	5.44	1.18	0.69
5-6cm	1.06	1.11	4.89	0.69
6-7cm				
7-8cm		n.d.		
8-9cm	1.06	5.65	1.12	0.72
9-10cm	0.94	5.18	1.11	0.72
10-11cm	0.90	5.07	1.07	0.72
11-12cm	0.60	4.51	0.91	0.75
12-13cm	0.81	6.00	1.29	0.74
13-14cm	0.65	5.18	1.03	0.76
14-15cm		n.d.		
15-16cm	0.66	5.51	0.92	0.78
16-17cm	0.59	5.09	0.89	0.77
17-18cm	0.54	4.81	0.82	0.78
18-19cm	0.52	4.51	0.76	0.78
19-20cm	0.49	4.16	0.81	0.76
20-21cm	0.27	2.58	0.47	0.78
21-22cm	0.46	3.81	0.74	0.76
22-23cm	0.47	3.97	0.79	0.76
23-24cm	0.39	3.37	0.72	0.75

Appendix Table 17: Sterol concentrations [µg] and β-sitosterol index in L13-04-2.

sample	Brassicasterol	β-Sitosterol	dinosterol	β-sit/(b-sit+brass+dino)
0-1cm	2.76	11.30	1.27	0.74
1-3cm	2.38	11.84	1.44	0.76
3-5cm	1.59	11.77	1.30	0.80
5-7cm	1.09	9.21	1.03	0.81
7-9cm	0.86	9.36	0.89	0.84
9-11cm	0.97	12.60	1.10	0.86
11-13cm	0.99	13.51	1.24	0.86
13-15cm	0.90	12.05	1.20	0.85
15-17cm	0.86	11.33	1.12	0.85
17-19cm	0.80	11.75	1.10	0.86
19-21cm	0.86	13.09	1.11	0.87
21-23cm	0.65	9.54	0.92	0.86
23-25cm	0.48	8.13	0.75	0.87

Appendix Table 18: Sterol concentrations [µg] and β-sitosterol index in L13-18-2.